Cell

Zebrafish use spectral information to suppress the visual background

Graphical abstract

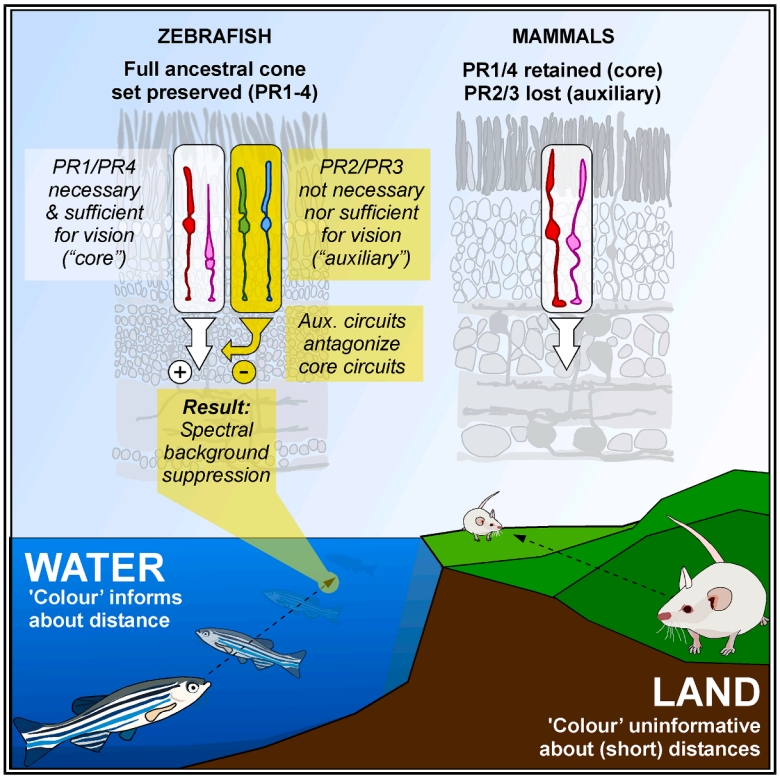

Highlights

- Zebrafish use fading spectral content in water to suppress visual background
- They do this by contrasting, not summing, inputs from distinct ancestral cone types
- Vertebrate cone diversity may reflect ancestrally aquatic "non-color" functions
- Mammalian cone loss may reflect rapid terrestrialization, not nocturnal ancestry

Authors

Chiara Fornetto, Thomas Euler, Tom Baden

Correspondence

C.Fornetto@sussex.ac.uk (C.F.), t.baden@sussex.ac.uk (T.B.)

In brief

Vertebrate eyes first evolved in water, where spectral content rapidly fades with distance. Zebrafish exploit this loss by antagonizing cone signals to suppress the background, pointing to distance estimation—rather than color—as an ancestral cone function.

Fornetto et al., 2025, Cell *188*, 1–17
December 24, 2025
https://doi.org/10.1016/j.cell.2025.10.009

CellPress

Cell

CellPress
OPEN ACCESS

Article

Zebrafish use spectral information to suppress the visual background

Chiara Fornetto,[1,*] Thomas Euler,[2] and Tom Baden[1,3,*]
[1]Sussex Neuroscience, School of Life Sciences, University of Sussex, Brighton BN1 9QG, UK
[2]Institute for Ophthalmic Research and Centre for Integrative Neuroscience, University of Tübingen, Tübingen 72076, Germany
[3]Lead contact
*Correspondence: C.Fornetto@sussex.ac.uk (C.F.), t.baden@sussex.ac.uk (T.B.)
https://doi.org/10.1016/j.cell.2025.10.009

SUMMARY

Vision first evolved in the water, where the spectral content of light informs about viewing distance. However, whether and how aquatic visual systems exploit this "fact of physics" remains unknown. Here, we show that zebrafish use "color" information to suppress responses to the visual background. For this, zebrafish divide their intact ancestral cone complement into two opposing systems: PR1/4 ("red/UV cones") versus PR2/3 ("green/blue cones"). Of these, the achromatic PR1 and PR4, which are retained in mammals, are necessary and sufficient for vision. By contrast, the color-opponent PR2 and PR3, which are lost in mammals, are neither necessary nor sufficient for vision. Instead, they form an "auxiliary" system that spectrally suppresses the "core" drive from PR1 and PR4. Our insights challenge the long-held notion that vertebrate cone diversity primarily serves color vision and further hint at terrestrialization, not nocturnalization, as the leading driver for visual circuit reorganization in mammals.

INTRODUCTION

In image-forming vision, information about two dimensions of space is hardwired into the retinotopic organization of eyes.[1] By contrast, information about distance must be inferred. Terrestrial tetrapods, including humans, address this problem computationally, through a combination of inner retinal object-segmentation circuits,[2–5] stereoscopy,[6,7] and cognitive strategies such as the use of pictorial cues.[8] However, image-forming eyes first evolved in the water,[9] which offers a much simpler cue for distance estimation: "whiteness" (Figure 1A).

Strong scattering and absorption of light in the water result in a rapid narrowing of spectral content with increasing viewing distance[12] (Figure 1A). The presence of spectrally broad light (i.e., "white") is therefore the exclusive remit of the foreground (Figures 1A and 1B; Video S1). Aquatic visual systems could exploit this "white effect," for example, by biasing retinal light responses toward spectrally broad input. Such a bias in the retinal output to the brain would almost inevitably lead to a foreground bias in visual behavior. However, whether and how aquatic visual systems use this inductive bias remains unknown.

In principle, a retinal white bias could be implemented by comparing achromatic ("grayscale") and chromatic (color) circuits[13,14] because these tend to respond in opposite directions to a change in spectral width (Figures 1A and 1B). Grayscale circuits (non-opponent) become progressively less active as the spectrum narrows (Figure 1A, middle) but color circuits (opponent) become more active. This is because the excitatory and inhibitory inputs to color-opponent circuits cancel under spectrally broad light,[15] and this cancellation wanes as the spectrum narrows toward its monochromatic point (Figure 1A, right). Any concurrent decrease in brightness and/or achromatic contrast[12] then accentuates these spectral differences: both strongly deteriorate grayscale signals, whereas color circuits are largely invariant to these orthogonal axes in stimulus space.

All required components for contrasting grayscale and color circuits are present in the larval zebrafish retina.[15,16] Like many fish, amphibians, reptiles, and birds,[9,17–19] this diurnal surface-dwelling teleost retains all four ancestral cone photoreceptor types (red, green, blue, and UV). In recognition of their deep conservation,[9,18–21] these four ancestral vertebrate cones were recently renamed[22] "photoreceptor types 1–4" (PR1–4), respectively. Of these, eutherian mammals including mice and humans retain PR1 and PR4 but lost PR2 and PR3.[9,18,22]

In the live eye, zebrafish PR1 (ancestral red cones) and PR4 (UV) are non-opponent, but PR2 (green) and PR3 (blue) are opponent due to outer retinal circuit interactions.[15] Accordingly, the four ancestral cone types of the zebrafish eye can be split into two grayscale (PR1/4) and two color channels (PR2/3). Net antagonistic wiring of PR1/4- versus PR2/3-driven circuits would therefore lead to a white bias in the retinal output, which, in turn, would mean that the visual information available for behavior is dominated by features from the (spectrally broader) foreground.

Here, we present direct evidence in support of this hypothesis. First, using two-photon imaging, we demonstrate that zebrafish vision is profoundly white biased. Second, using genetic ablation

Please cite this article in press as: Fornetto et al., Zebrafish use spectral information to suppress the visual background, Cell (2025), https://doi.org/10.1016/j.cell.2025.10.009

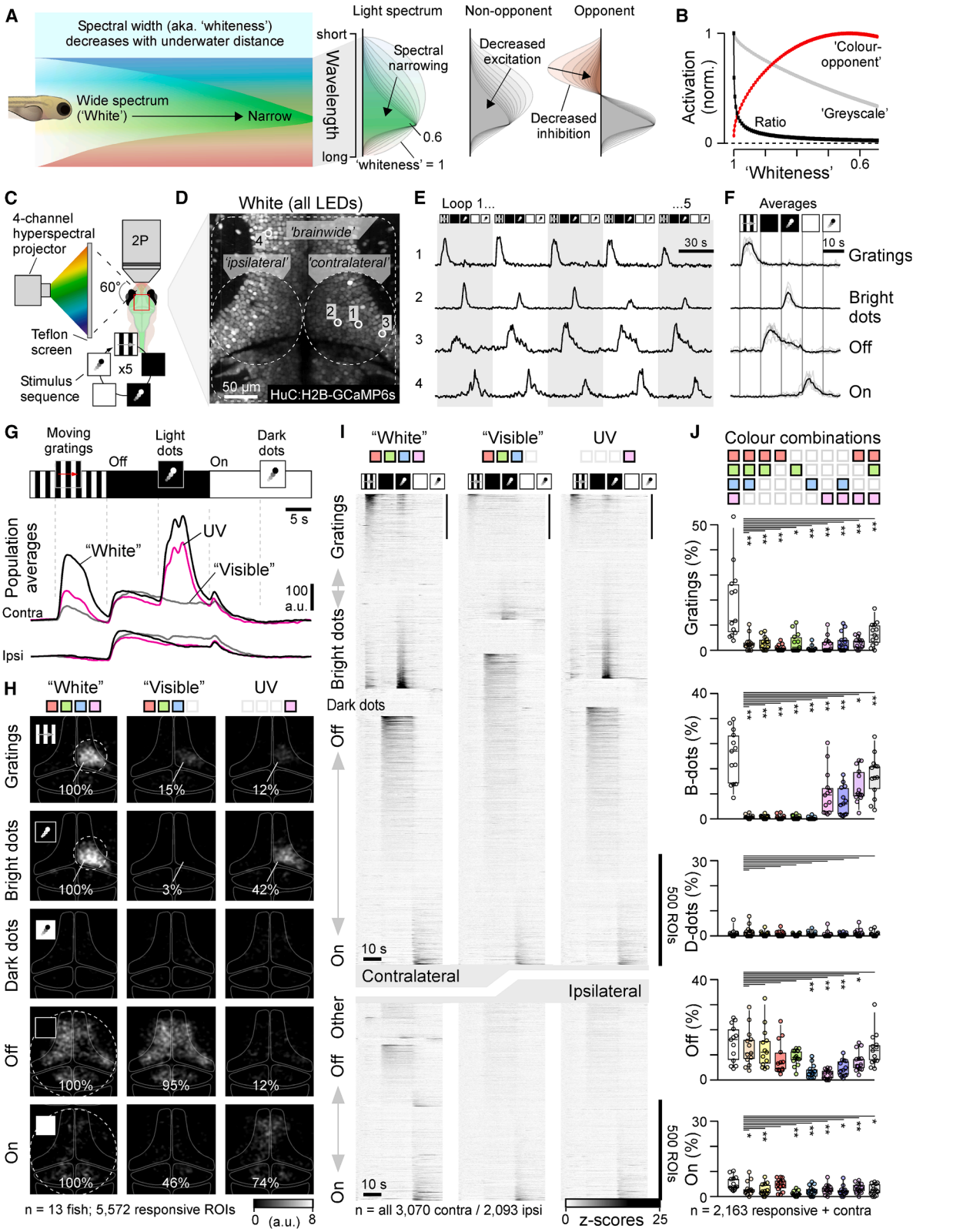

(legend on next page)

of individual and combinations of cone types, we show that this white bias emerges from the systematic contrasting of PR1/4 versus PR2/3 circuits. Specifically, we show that PR1 and PR4 are necessary and sufficient for spatiotemporal vision, whereas PR2 and PR3 are neither necessary nor sufficient for vision and instead suppress PR1/4 circuits. Third, we show that the PR2 and PR3 systems act in mutual opposition. Fourth, we confirm our results at the level of three ancient and highly conserved visual behaviors: spontaneous swimming in the presence and absence of light, phototaxis, and the optomotor reflex.

Together, our results challenge the textbook notion that vertebrate photoreceptors act in concert to drive visual behavior, while their opposition serves color vision.[14,23] Instead, we show that zebrafish cone circuits are fundamentally wired to compete.[9] Although corresponding circuit architectures in other fishes remain unknown, our results tentatively support an alternative view on the retina's originally aquatic circuit architecture, provide insights into the evolution of vertebrate vision,[24] and hint at terrestrialization[25]—not nocturnalization[26]—as the leading driver of visual circuit reorganization in early *Synapsida*, the ancestors of all mammals.[27–29]

RESULTS

Zebrafish vision is white biased

To assess how zebrafish process spectral content in spatiotemporal visual stimuli, we used two-photon imaging of light-evoked neural activity in the tectum, the principal retinorecipient area of the teleost brain (Figures 1C and 1D; Video S2). Stimuli were projected onto a lateral screen using a custom "four-color hyperspectral" stimulator,[11] with wavelengths approximating the spectral sensitivity peaks of the cones *in vivo*[15] (from "red" to "UV": 587, 470, 422, and 373 nm, respectively). Relative stimulus intensities were adjusted to follow the natural spectral distribution of daylight in the zebrafish habitat[30] (from red to UV: 1200, 600, 300, and 150 μW, respectively; Figures S1A–S1C). Accordingly, concurrent activation of all four spectral channels approximated "zebrafish-white" (achromatic), whereas selective activation of subsets could be used to present various "colored" (chromatic) stimuli.

Throughout, we focused on three universal aspects of visual circuit computation: (1) light detection (widefield on/off), linked to, e.g., phototaxis[31,32] and visuomotor reflexes[33]; (2) widefield motion (large moving gratings), linked to, e.g., optomotor/optokinetic reflexes[34]; and (3) local object motion (small moving dots), linked to, e.g., visual prey capture.[35–37]

Of these, the detection of light (or its absence) is principally possible with any photosensitive system, including extraocular, while the latter two require retinal processing (hereafter referred to as "spatiotemporal vision"). To probe the above-described stimulus space, we used a stimulus sequence comprising widefield moving gratings as well as small light and dark moving dots superimposed on dark and bright backgrounds, respectively (Figures 1E–1G). When presented in zebrafish-white, individual tectal neurons responded selectively to specific aspects of this stimulus sequence over repeated trials (Figures 1E and 1F): moving gratings and bright moving dots on a dark background (hereafter "bright dots") elicited large numbers of responses, whereas dark dots on a bright background (hereafter "dark dots") triggered few responses, if any. Together, responses to spatiotemporally patterned stimuli were consistently restricted to the retinotopically aligned base of the tectum, in line with direct drive from the stimulated eye (Figures 1G and 1H, cf. Figures 1C and 1D). By contrast, on/off responses (i.e., light detection) were routinely observed all over the brain, with no obvious contralateral or retinotopic bias.

Next, we repeated this experiment using various shades of colored light (Figures 1G–1J). This revealed a striking white bias in the representation of spatiotemporal stimuli but not in basic light detection. For example, "visible light" (red, green, and blue [RGB]), lacking the ultraviolet (UV) component, was far less effective at eliciting spatiotemporal pattern responses compared with white light (i.e., RGBU; cf. Figures S1A–S1F): omission of UV, which accounts for less than 7% of the total stimulus power in white, resulted in an 85% loss of grating responses and a 97% loss of bright-dot responses (i.e., white-corrected efficiencies of 15% and 3%, respectively). Conversely, activating the UV channel alone yielded a white-corrected efficiency of only 12% for gratings and 42% for bright dots (Figures 1G–1J).

Other wavelength combinations yielded comparable results (Figures 1J and S1F): relative to white, the preponderance of both grating and bright-dot responses was strongly and significantly reduced in all non-white stimulus conditions. For gratings, the most effective non-white stimulus was "RGU" (red, green, and UV), with a white-corrected mean efficiency of 36%, despite a light power loss of less than 9%. Spectrally narrow stimulation was even less effective, with red, green, or "blue" channels

Figure 1. Zebrafish vision is white biased

(A and B) Illustration of how spectrally broad (white) light fades with underwater distance and how idealized "color-opponent" and grayscale detectors respond to corresponding changes in spectral width (STAR Methods; see also Video S1).

(C) Setup for two-photon imaging of tectal neurons in larval zebrafish[10] during presentation of "4-color spatial stimuli"[11].

(D–F) Representative scan with annotated brain regions and example regions of interest (ROIs) (D) showing single-trial (E) and averaged (F) responses to a battery of widefield and spatiotemporal stimuli.

(G) Average responses to the same stimulus sequence of all contralateral (top) and ipsilateral (bottom) ROIs. ROIs from 13 fish when presented in white (black line), visible light (gray line), and UV (pink line).

(H) Spatial response distribution within the brain. Percentages indicate the average abundance of responses relative to white (=100%).

(I) All contralateral (top) and ipsilateral (bottom) responses to white, visible, and UV light, sorted by response type (cf. Video S2).

(J) Statistics for the number of responses to each stimulus and color combination (STAR Methods). Statistical comparisons against white (1st column) based on one-tailed paired Wilcoxon rank-sum test with Bonferroni correction for multiple comparisons (*$p < 0.05$; **$p < 0.01$; no asterisk, $p > 0.05$). Full statistics in Table S1A.

See also Figure S1.

Please cite this article in press as: Fornetto et al., Zebrafish use spectral information to suppress the visual background, Cell (2025), https://doi.org/10.1016/j.cell.2025.10.009

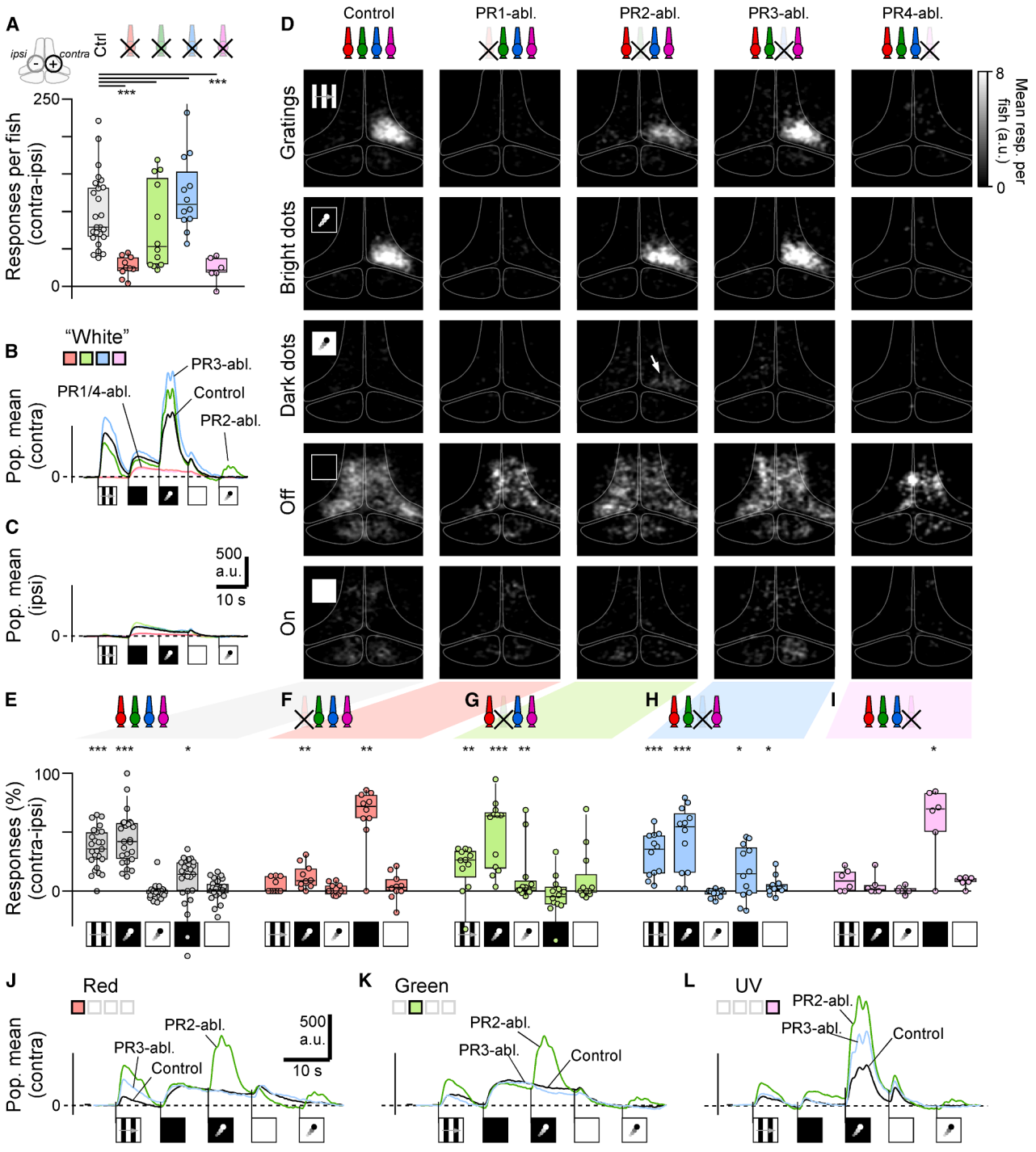

Figure 2. Spatiotemporal vision does not require PR2 or PR3

(A) Number of contralaterally responsive ROIs per fish (STAR Methods) during presentation of our battery of spatiotemporal stimuli (cf. Figure 1) presented in white, minus the corresponding number of ipsilateral responses. From left: controls, and animals following the genetic ablation of PR1 (red), PR2 (green), PR3 (blue), and PR4 (UV) cones (for nomenclature, see Baden et al.[22]). Statistics based on two-tailed Wilcoxon rank-sum test with Bonferroni correction for multiple comparisons (details in Table S1B).

(B–D) As in Figures 1G and 1H, but only for white responses of controls and following ablation of different cones. Arrow in (D) highlights the unmasking of dark-dot responses (see also Figures S2A–S2E).

(E–I) Statistics for contralateral responses per fish, corrected for ipsilateral responses. Shown are the numbers of responsive ROIs per stimulus as a percentage of all responsive ROIs. Note that this normalization overemphasizes response numbers in poorly responsive animals (e.g., following PR1/4 ablation). Uncorrected

(legend continued on next page)

Please cite this article in press as: Fornetto et al., Zebrafish use spectral information to suppress the visual background, Cell (2025), https://doi.org/10.1016/j.cell.2025.10.009

individually eliciting fewer than 5%, 17%, and 3% grating responses, respectively, relative to white. The most reliable bright-dot responses were also elicited by white light; however, unlike for gratings, and in line with previous work,[30,35,38] their presence or absence was, in addition, specifically related to the presence or absence of UV light. The most effective non-white condition was, again, RGU, with a white-corrected efficiency of 72%. RU and UV-only stimulation were second and third, with 55% and 42% efficiency, respectively. In the absence of UV light, independent of which other wavelengths were present, bright-dot responses were elicited with a white-corrected efficiency of 5% at most. These results demonstrate that responses to spatiotemporally patterned stimuli are "white biased" far beyond what could be reasonably explained by stimulus intensity alone.

Unlike responses to patterned stimuli, neither off nor on responses were specifically tuned to white. For example, in both cases, the response to red-only (R) stimulation was statistically indistinguishable from the white response (Figure 1J).

We conclude that in the larval zebrafish brain, the representation of spatiotemporally patterned stimuli such as drifting gratings or prey-like moving dots, but not of basic light-dark transitions, is under intimate control of spectrally competing circuits that suppress responses to non-white stimuli.

Spatiotemporal vision does not require PR2 or PR3

To pinpoint the origin of the white bias, we generated transgenic zebrafish lines where each of the four types of cones could be ablated[15,39] via cell-type-specific expression of bacterial nitroreductase,[40] which converts the otherwise harmless prodrug metronidazole into a cytotoxin. We then presented acutely cone-type-ablated zebrafish with the same white stimulus sequence. This directly confirmed our hypothesized[9] circuit architecture: ablation of PR1 (red) or PR4 (UV), but not of PR2 (green) or PR3 (blue), resulted in a profound loss in overall visual responsiveness (Figure 2A). This loss was consistently characterized by a near-complete cessation of spatiotemporal pattern responses, but only moderate effects on off and on responses (Figures 2A–2I and S2).

First, ablation of PR1 completely abolished grating responses but spared a small, but significant, number of bright-dot responses (Figures 2B–2F). Second, PR4 ablation completely abolished both grating and dot responses (Figures 2B–2D and 2I). Third, both grating and bright-dot responses persisted after the ablation of PR2 or PR3 (Figures 2B–2D, 2G, and 2H). Of these, response numbers were statistically indistinguishable from controls, except for PR2-ablated grating responses, which were slightly but significantly reduced ($p_{B\text{-}dots}$ = 0.24 [PR2] and 0.43 [PR3]; $p_{Gratings}$ = 0.013 [PR2] and 0.23 [PR3], one-tailed Wilcoxon rank-sum test). Moreover, PR2 ablation unmasked previously absent responses to dark dots ($p_{D\text{-}dots}$ = 0.007 [PR2] and 0.043 [PR3]).

Ablation of PR2 or PR3 also led to various types of increases in the overall "population response" to spatiotemporally patterned stimuli, which considers both the number of responsive neurons and their individual response amplitudes (Figures 2B and 2C). These effects tended to increase when using spectrally narrow light (Figures 2J and 2L) instead of white. For example, PR3 ablation accentuated responses to red light gratings (Figure 2J) and to UV bright dots (Figure 2L). The same responses were also increased following PR2 ablation; however, in this case, effects were more widespread and notably included the unmasking of dark-dot responses at all tested wavelengths (Figures 2J–2L), as well as increased spatiotemporal pattern responses under UV light (Figure 2L), where PR2 itself is insensitive (Figure S1E). The latter observation implies that PR2 indirectly suppresses UV responses, for example, by interaction with PR3 (Figure S1E).

Other than for the above-described effects on spatiotemporal pattern responses, the representation of off and on stimuli mostly persisted after individual cone-type ablations (Figures 2B–2I), and their contralateral bias tended to be weak (off) or altogether absent (on), including in the control condition (Figures 2D–2H). Nevertheless, the only significant contralateral changes were again in the case of PR2 and PR3 ablation. The weak contralateral off bias was selectively lost following PR2 ablation, whereas PR3 ablation uniquely unmasked a small but significant contralateral bias in on responses (Figure 2H).

Together, the results from these ablation experiments strongly suggest that the processing of different types of basic visual stimuli is specifically linked to distinct subsets of cones.[9] In particular, the profound overall loss in responses to spatiotemporally patterned stimuli in the absence of PR1 or PR4 indicates that these two cones are essential for "normal" vision. Conversely, the persistence of spatiotemporal pattern responses following the ablation of PR2 or PR3—coupled with the observation that responsiveness to spatiotemporal patterns tended to increase—and that novel response types could be unmasked, indicates that these cones normally suppress rather than drive retinal output.

PR1 and PR4 are necessary and sufficient for spatiotemporal vision

The inferred opposite roles of PR1/4 and PR2/3 circuits in vision were further directly supported by the results of double-ablation experiments: concurrent ablation of PR1 and PR4 resulted in a complete cessation of contralateral spatiotemporal pattern responses (Figures 3A–3F and S3). Conversely, spatiotemporal pattern responses persisted after the concurrent ablation of PR2 and PR3 ($p_{B\text{-}dots}$ = 0.14; $p_{Gratings}$ = 0. 14; Figures 3G and S3). Moreover, as previously observed for PR2 ablation (Figure 2), dark-dot responses were unmasked ($p_{D\text{-}dots}$ = 0.023; Figures 3B and 3G) and the contralateral bias for off responses was lost. However, concurrent ablation of PR2 and

numbers are shown in Figures S2F–S2K. Statistics are per stimulus condition, comparing the numbers of contralateral versus ipsilateral responses, based on one-tailed Wilcoxon rank-sum test (*$p < 0.05$; **$p < 0.01$; ***$p < 0.001$; no asterisk, $p > 0.05$; cf. Table S1B).
(J–L) As in (B), but shown for red (J), green (K), and UV stimulation (L).
See also Figure S2.

Please cite this article in press as: Fornetto et al., Zebrafish use spectral information to suppress the visual background, Cell (2025), https://doi.org/10.1016/j.cell.2025.10.009

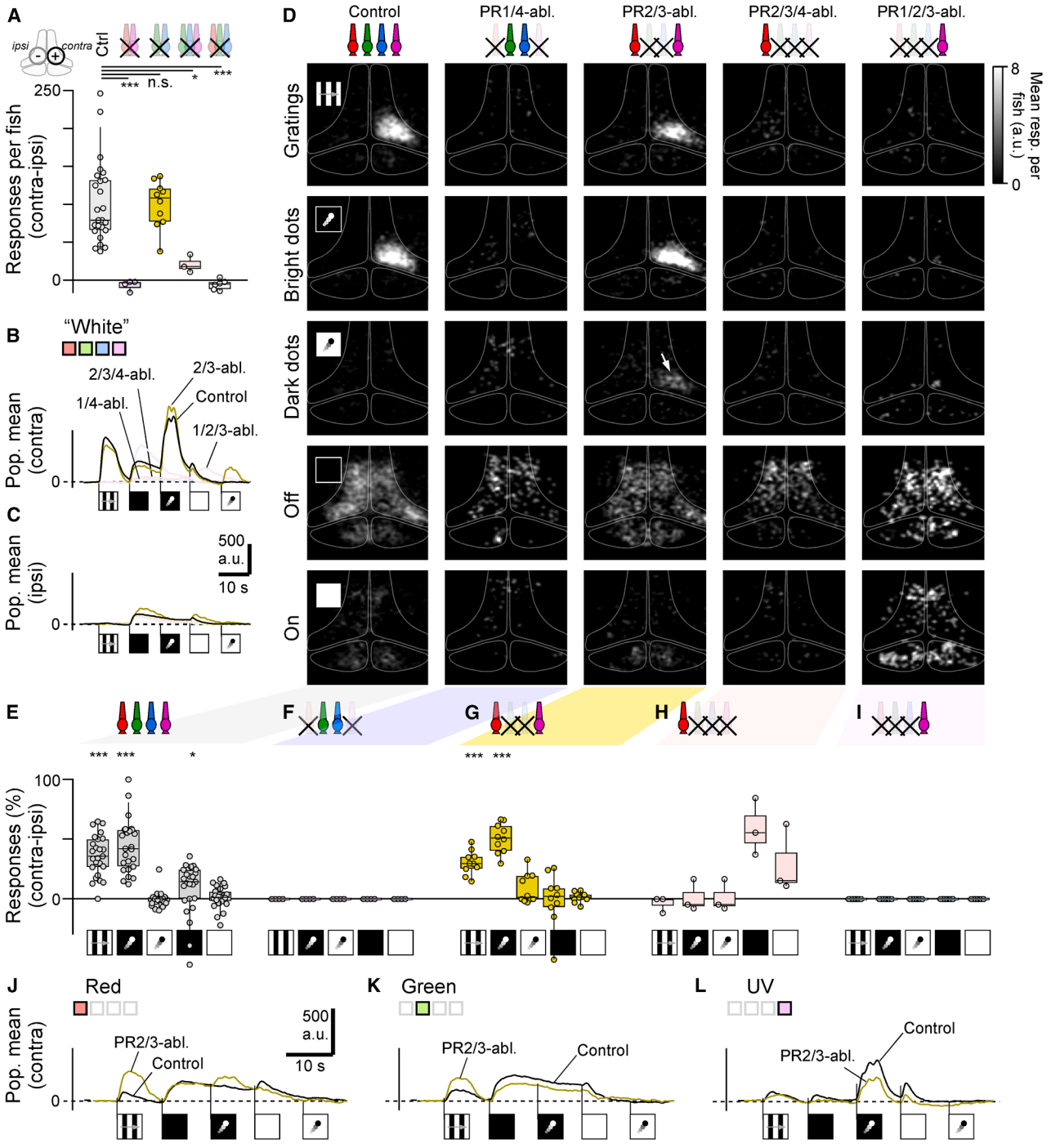

Figure 3. PR1 and PR4 are necessary and sufficient for spatiotemporal vision

(A–L) As in Figures 2A–2L, but shown for different cone ablations. In each set of panels, from left: control, PR1/4 double ablated, PR2/3 double ablated, PR2/3/4 triple ablated, and PR1/2/3 triple ablated. Statistics (E–L) annotated in Table S1B. For clarity, (J)–(L) only show controls and PR2/3 double-ablated data. For convenience, control data from Figure 2 is repeated.

See also Figure S3.

PR3 ameliorated the overall "inflation" of spatiotemporal pattern responses that was observed following individual cone-type ablations (Figures 3B and 3J–3L, cf. Figures 2B and 2J–2L).

Next, even though concurrent ablation of PR1 and PR4 approximately recapitulated their individual ablation phenotypes, the normal functioning of the visual system was contingent on their

Please cite this article in press as: Fornetto et al., Zebrafish use spectral information to suppress the visual background, Cell (2025), https://doi.org/10.1016/j.cell.2025.10.009

CellPress
OPEN ACCESS

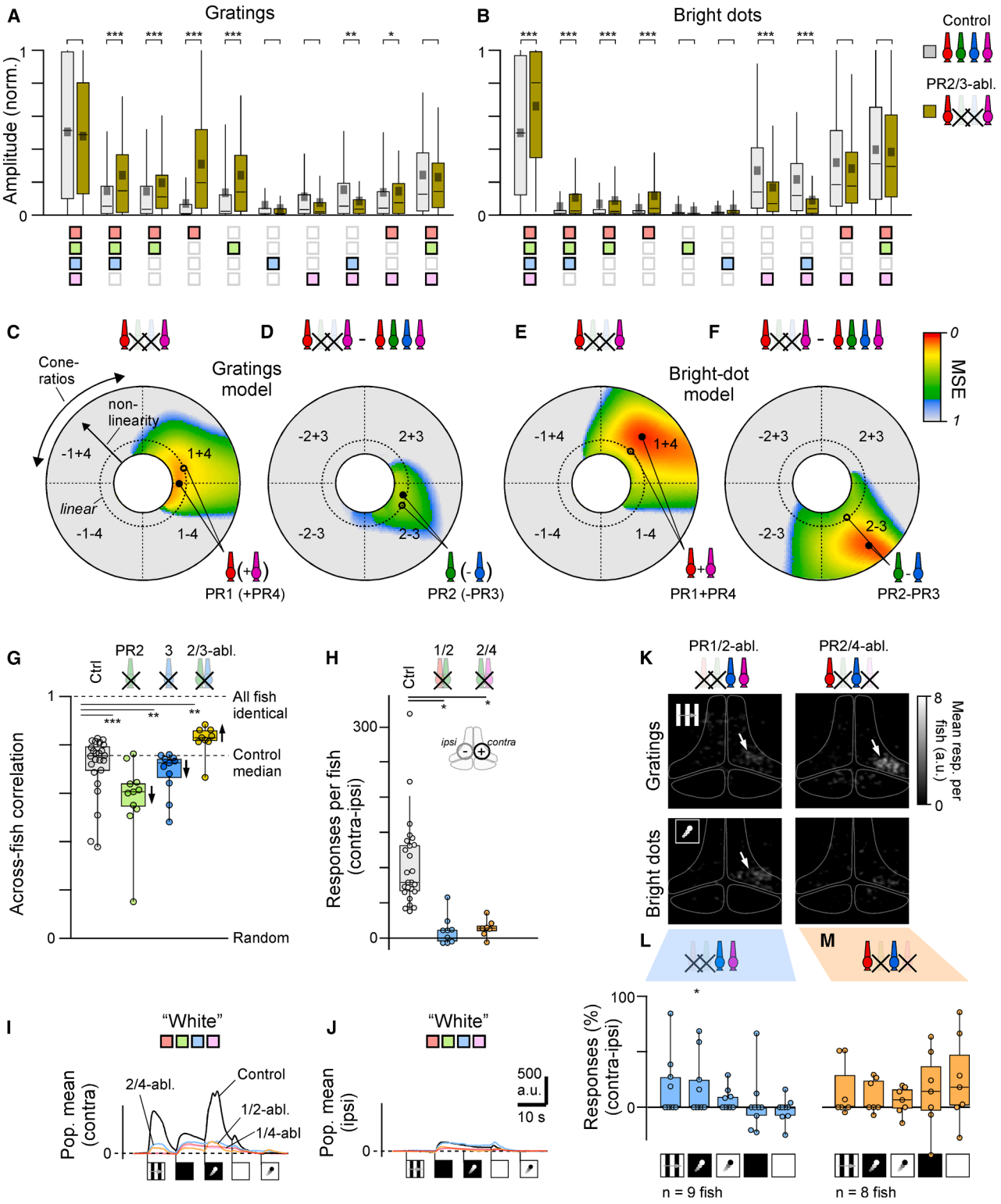

Figure 4. PR2 and PR3 circuits act in mutual competition

(A and B) Normalized spectral response amplitudes of contralateral ROIs that responded to gratings (A) or bright dots (B) in controls (gray) and in PR2/3 double-ablated animals (yellow). Details in STAR Methods. The full PR2/3 double-ablated data are summarized in Figure S4A, and distributions for dark dots and off/on stimuli are shown in Figures S4B–S4D, respectively. Note that response amplitudes for non-white conditions tended to increase toward "white-like" levels

(legend continued on next page)

Please cite this article in press as: Fornetto et al., Zebrafish use spectral information to suppress the visual background, Cell (2025), https://doi.org/10.1016/j.cell.2025.10.009

joint presence: triple ablations, leaving only PR1 (Figure 3H) or only PR4 in place (Figure 3J), both resulted in a complete loss of pattern responses.

Together, the results from this series of ablation experiments strongly suggest that the joint presence of both PR1 and PR4 is necessary and sufficient for normal spatiotemporal pattern vision. Conversely, the presence of PR2 and PR3 appeared to be inessential for spatiotemporal vision (at least for the tested stimulus space), and their individual absence accentuated various aspects of visual responses.

The picture that emerges is one where the four ancestral types of cones of the vertebrate eye can be divided into two opposing systems: PR1 and PR4 drive vision, but PR2 and PR3 suppress—and thereby regulate—visual circuits. Moreover, the "inflated" response phenotypes following individual PR2 or PR3 ablation, compared with PR2/3 double ablation, further implies that PR2 and PR3 normally interact among themselves before imparting their regulatory functions to PR1 and PR4 circuits.

PR2 and PR3 cause the white bias in zebrafish vision

Next, we systematically combined cone ablations and spectral stimulation to elucidate how PR2 and PR3 regulate vision. To this end, we concurrently ablated PR2 and PR3 and presented the same battery of spectral combinations that was previously used to probe controls (cf. Figures 1J and S1F). This revealed that, for both gratings and bright dots, PR2/3 double-ablated animals were systematically retuned relative to controls (Figures 4A, 4B, and S4A–S4D). In both cases, spectral responses were shifted toward longer wavelengths at the expense of shorter wavelengths. Moreover, the white bias was largely lost. For example, unlike in controls, grating responses to red-only stimulation were statistically indistinguishable from white stimulation in PR2/3-ablated animals ($p = 0.11$, paired Wilcoxon rank-sum test, one tailed). In addition, the spectral tuning functions of gratings and off responses were now comparable (Figure 4A, cf. Figure S4C). We conclude that the striking white bias in zebrafish vision (Figure 1) largely stems from the net-suppressive circuit interactions of PR2 and PR3 on retinal output.

PR2 and PR3 circuits act in mutual competition

We next used the spectral tuning functions of control and PR2/3 double-ablated animals to computationally infer the underlying cone contributions to grating and dot responses. This was possible by using computed individual cone activations per spectral stimulus condition as the basis functions (cf. Figures S1A–S1E). From here, we used a two-step cone-combinatorial model[15,41] (Figures 4C–4F). Data from PR2/3 double-ablated animals were used to infer PR1 versus PR4 weights (Figures 4C and 4E), while the differences between controls and double-ablated animals were used to infer PR2 and PR3 weights (Figures 4D and 4F). Together, this added further support to the notion that PR1 and PR4 act in concert, while PR2 and PR3 act in mutual opposition.

For gratings, spectral responses of PR2/3-ablated animals were best approximated by a sublinear drive from PR1 alone (87.3% explained; Figures 4C and S4E). Small additional contributions from PR4 achieved near-equivalent and linear fits (82.7%; Figure 4C, open symbol). Conversely, the spectral differences between double-ablated and control responses were best explained by net-positive contributions from PR2 but net-negative contributions from PR3 (61.3%; Figures 4D and S4G). Likewise, bright-dot tuning functions were best explained by a net positive contribution from both PR1 and PR4 (95.1%; Figures 4E and S4F) but an opposing contribution from PR2 minus PR3 (92.4%; Figures 4F and S4H). Accordingly, both response types point to a single underlying circuit architecture: joint drive from PR1 and PR4 and mutual opposing regulation from PR2 and PR3. The main difference between grating and bright-dot circuits appeared to be that the former is PR1/2 dominant and (sub)linear, while the latter is PR4/3 dominant and supra-linear.

Beyond gratings and bright dots, the newly unmasked responses to dark dots also followed a bright-dot-like "U-shaped" spectral tuning curve, indicative of concomitant PR1 plus PR4 drive (Figure S4B). In this case, the sparsity of dark-dot responses in control animals precluded estimating relative PR2/3 contributions. However, the observation that dark-dot responses were selectively unmasked following PR2 ablation (Figure 2G), but not PR3 ablation (Figure 2H), points to an unequal suppressive action of PR2 versus PR3 systems in controls.

Concurrent ablation of PR2 and PR3 restores the lost balance that follows single-cone ablations

If PR2 and PR3 act in mutual opposition to regulate PR1/4-driven circuits, then selective ablation of only parts of such a regulatory system should result in a poorly balanced visual circuit. However, this balance should improve if the regulatory system is ablated in its entirety. For example, individual differences between animals are likely to be more pronounced if the PR2/3 system is damaged, but less so if it is missing altogether. This effect was in

following PR2/3 ablation—particularly notable for red stimulation of gratings (A, 4th pair of bars). Statistical comparisons in (A) and (B) based on one-tailed Wilcoxon rank-sum test with Bonferroni correction for multiple comparisons (*$p < 0.05$; **$p < 0.01$; ***$p < 0.001$; no asterisk, $p > 0.05$). Full statistics in Table S1C.
(C–F) Results of two-step cone-combinatorial model (STAR Methods) that captures the spectral tunings of grating (C and D, cf. A) and bright-dot responses (E and F, cf. B) based on spectral tunings of cones (cf. Figures S1D and S1E). Heatmaps summarize mean squared error (MSE) between a target-tuning function and the tuning of each possible cone combination, normalized between 0 (perfect fit) and 1 (no fit). Distance from the center denotes the linearity of the model, from sublinear to supra-linear toward the outside. The dashed circle denotes the linear point, while closed and open circles denote the best fit overall and the best linear fit, respectively. Corresponding best fits are shown in Figures S4E–S4H. Inferred cone ratios (2 s.f.) as follows: gratings: 0.99PR1:−0.1PR4 (linear: 0.75PR1:0.25PR4); 0.88PR2:−0.12PR3; dots: 0.45PR1:0.55PR4; 0.42PR2:−0.58PR3.
(G) Response homogeneity (STAR Methods) across the population of control animals and following ablation of PR2, PR3, and PR2/3 cones. Statistics based on one-tailed Wilcoxon rank-sum test of each ablation condition relative to controls, with Bonferroni correction for multiple comparisons. pPR2 = 0.000036, pPR3 = 0.0004, pPR2/3 = 0.0061.
(H–M) As in Figures 2A–2I, shown for controls and two new ablation combinations: PR1/2 (left) and PR2/4 (right). Full statistics in Table S1B.
See also Figures S4 and S5.

Please cite this article in press as: Fornetto et al., Zebrafish use spectral information to suppress the visual background, Cell (2025), https://doi.org/10.1016/j.cell.2025.10.009

CellPress
OPEN ACCESS

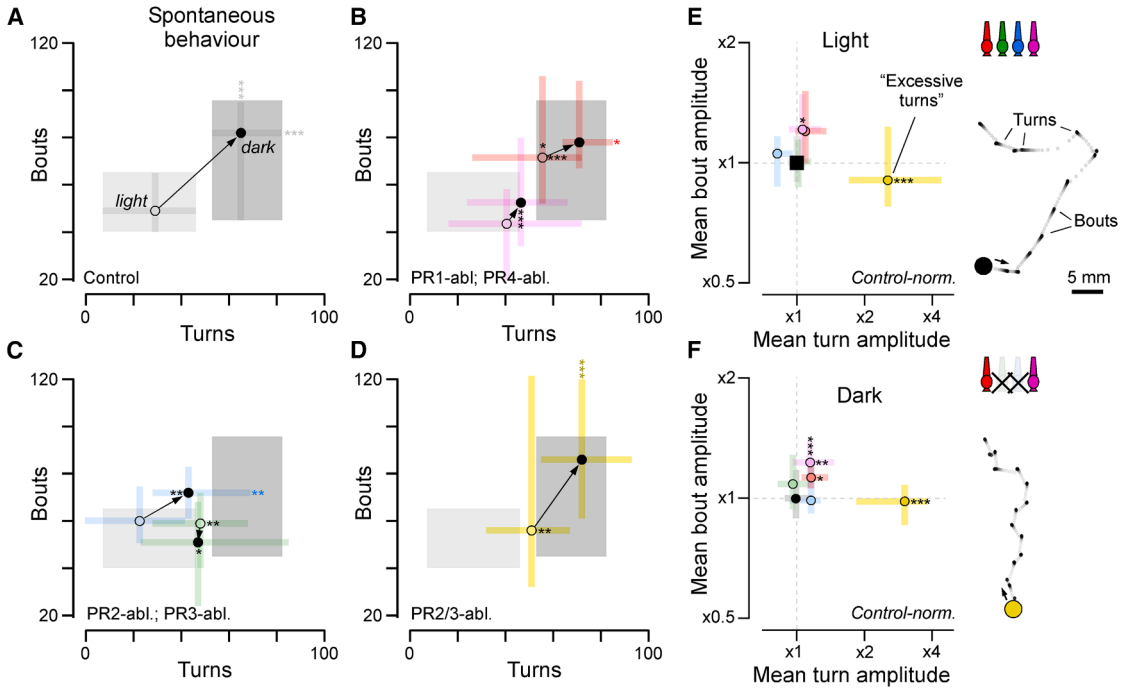

Figure 5. Cone-type-specific deficits in spontaneous swimming behavior

(A–D) Spontaneous movement statistics (STAR Methods) of free-swimming fish in continuous light (open symbols) or dark (closed symbols). Shown are controls (A), PR1- and PR4-ablated (B), PR2- and PR3-ablated (C), and PR2/3 double-ablated animals (D). Shadings denote interquartile ranges of light and dark behaviors in controls. For clarity, only medians and interquartile ranges are plotted. Two sets of comparisons were performed using one-tailed Wilcoxon rank-sum tests: "within metric," comparing control versus ablation conditions (black asterisks within the corresponding range bars), and "within condition" comparing light versus dark (colored asterisks outside of the error bars). Full statistics in Table S2A.

(E and F) Quantification of each populations' median bout and turn amplitudes, normalized to controls (=1). Full statistics in Table S2B.

See also Figure S6.

fact readily observed in the scattered response distributions across PR2 or PR3 single-ablated animals (Figures 2G and 2H) compared with controls (Figure 2E), as well as the notably tighter distribution of responses across animals for PR2/3 double-ablated animals (Figure 3G). To quantify this effect, we computed the correlation of each animal's response distribution (i.e., the relative responsiveness to gratings, bright dots, dark dots, off, and on) against the remainder of the population, such that 1 and 0 indicate perfectly homogeneous and random populations, respectively (Figure 4G). This confirmed that both PR2 and PR3 single-ablated animals were significantly more heterogeneous than controls, whereas PR2/3 double-ablated animals were significantly more homogeneous.

To further explore this idea, we carried out two additional sets of double-ablation experiments, but this time "half-ablating" both the core and the regulatory systems. We reasoned that half-ablating the core system (i.e., PR1 or PR4, but not both) should disrupt spatiotemporal pattern responses, while half-ablating the regulatory system (here PR2 but not PR3) should then partly counteract this disruption. This is indeed what we found. Both PR1/2 and PR4/2 double-ablated animals were less responsive than controls but more responsive than PR1 or PR4 single-ablated animals (Figures 4H–4K, cf. Figures 2 and S5). Moreover, strikingly, these "half-ablated" animals were exceptionally heterogeneous: following either ablation pair, approximately half of the animals were entirely unresponsive to any spatiotemporal patterns, while the other half displayed response levels that were well within the normal distribution of controls (Figures 4L and 4M, cf. Figure 2E). These results underscore the antagonistic balance within the PR2/3 system, such that its experimental disruption can lead to high phenotypic diversity.

Cone ablations lead to type-specific deficits in spontaneous swimming behavior

We next explored whether and how different cone circuits can be linked to behavior. We began with a characterization of spontaneous behavior by filming free-swimming individuals in constant light or constant dark (Figures 5, S6A, and S6B). This revealed that all tested ablations led to cone-type-specific behavioral deficits in spontaneous swimming.

As shown previously,[42] control animals exhibited notably more swim bouts and spontaneous turns in the dark compared with the light (Figure 5A). By contrast, this light-dependent phenotype was largely lost following the ablation of PR1 or PR4 (Figure 5B). Instead, PR4-ablated animals behaved as if always in the light, while PR1-ablated animals behaved as if always in the dark. These results support the notion that the concurrent presence of both cones is required for normal visual behavior, and further hint that, in the intact system, their relative activations contribute to determining behavioral state.

Please cite this article in press as: Fornetto et al., Zebrafish use spectral information to suppress the visual background, Cell (2025), https://doi.org/10.1016/j.cell.2025.10.009

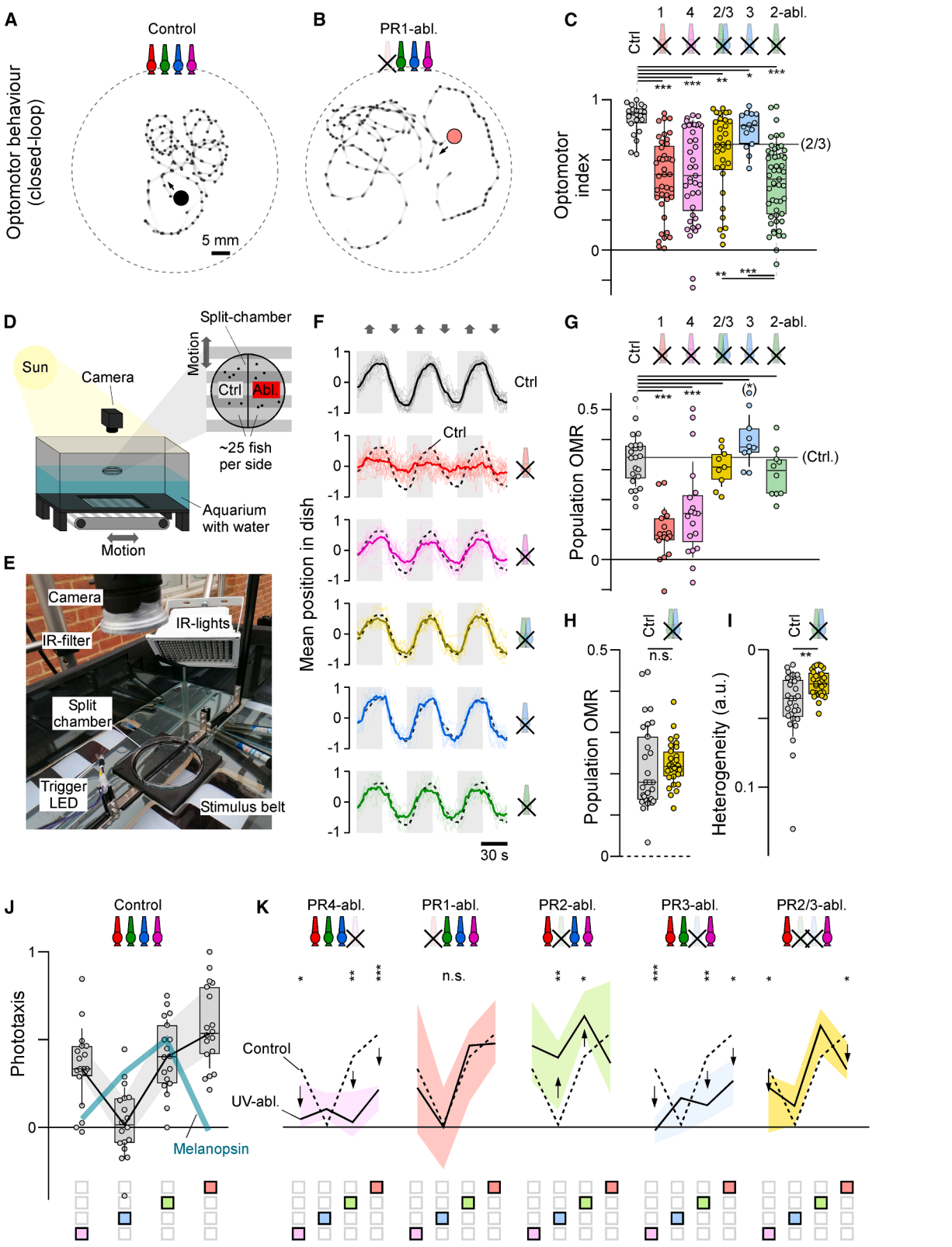

(legend on next page)

Next, unlike for PR1 or PR4, PR3-ablated animals behaved normally in the light but failed to fully reach control-like activity levels in the dark. Conversely, PR2-ablated animals always exhibited intermediate activity levels (Figure 5C). PR2 and PR3 phenotypes were, however, "rescued" in PR2/3 double-ablated animals, which, despite an elevated turn rate in the light, exhibited the most control-like behavioral performance overall among all tested ablations (Figure 5D). These results add direct support to the notion that PR2/3 compete to regulate rather than drive vision.

However, despite their approximately control-like spontaneous activity levels, PR2/3 double-ablated animals did exhibit another, unique behavioral deficit: they "over turned" (Figures 5E and 5F). Independent of illumination, these animals exhibited more than 2-fold-larger mean turn amplitudes compared with any other tested population. It appears that, in the absence of the "regulatory" PR2/3 system, zebrafish struggle to reliably swim in a straight line over successive bouts.

Cone-type-specific optomotor deficits

We next tested the effects of cone ablations on optomotor performance, a probably ancestral reflex that helps animals to stabilize their body position relative to the visual environment.[34] We started by using an "indoor" closed-loop setup,[43] where the orientation of sideways-drifting gratings constantly updated to align with the primary body axis. In this environment, free-swimming control fish perpetually turned toward the widefield drift, which leads to "circling behavior" (Figure 6A). By contrast, ablation of different cone types led to various types of behavioral deficits (Figures 6B and 6C).

In general, deficits in the central representation of grating responses (Figures 2 and 3) were a strong predictor of indoor optomotor performance: PR1-, PR2-, and PR4-ablated animals exhibited poor optomotor responses, in line with the complete (PR1/4; Figures 2D, 2F, and 2I) or moderate (PR2; Figures 2D and 2G) loss of grating responses in the brain. By contrast, PR3-ablated animals displayed no significant defects, in line with their intact central representation of moving gratings (Figures 2D and 2H). Moreover, as for spontaneous swimming (Figures 5C and 5D), double ablation of PR2/3 partially rescued the PR2 single-ablation phenotype. This behavioral pattern also implies that, in the intact system, PR2 circuits normally suppress PR3 circuits, which, in turn, suppress optomotor circuits: the only experimental difference between PR2 and PR2/3 double-ablated animals is the presence of PR3 cones. Accordingly, and perhaps counterintuitively, the poor behavioral performance of PR2-ablated animals must be attributed to a disinhibited net-suppressive action of PR3 cones.

Next, the presence of high-contrast moving gratings also largely overrode the spontaneous over-turning phenotype of PR2/3 double-ablated animals (Figure S6C, cf. Figures 5E and 5F). In fact, all tested ablation variants turn less frequently than controls (Figure S6D), but all but PR3 also partly compensated for this reduction by increasing turn amplitudes (Figure S6C).

Moreover, PR4-ablated animals alone also exhibited reduced bout rates (Figure S6D). The latter observation further hints that, beyond visual deficits, the poor optomotor performance of PR1- and PR4-ablated animals may also be partly related to systematic changes in behavioral state: PR4 ablation tended to reduce behavioral activity, whereas PR1 ablation tended to result in hyperactivity (Figures 5B, 5E, 5F, S6C, and S6D).

Only PR1 and PR4 ablation leads to optomotor defects under natural daylight

Encouraged by the close alignment between the representation of moving gratings in the brain (Figures 2 and 3) and optomotor performance under artificial but controlled indoor conditions (Figures 6A–6C), we next wondered how controls and animals with different cone types ablated would perform under more natural, outdoor conditions. For this, we devised an outdoors optomotor arena based on an open-top, water-filled aquarium suspended above a motorized conveyor belt for stimulus presentation (Figures 6D and 6E; Video S3; STAR Methods). The arena was placed outdoors in the midday sun. We then suspended a split chamber, with ~25 controls and populations of cone-ablated fish each, on either side of the water surface to internally control for natural changes in lighting conditions over the course of experiments (e.g., clouds and shadows). We then moved the conveyor belt back and forth and quantified the mean position of all fish per side over time (Figure 6F). In general, the results from this more naturalistic "outdoor" optomotor paradigm mirrored—and indeed accentuated—behavioral differences observed using the indoor setup (Figure 6G, cf. Figure 6C). Most importantly, now only PR1- and PR4-ablated animals

Figure 6. Cone-type-specific deficits in optomotor behavior and phototaxis

(A and B) Example movement trajectories in closed-loop optomotor assay[43] for a control (A) and a PR1-ablated animal (B).

(C) Quantification of optomotor performance (STAR Methods) across conditions. Statistics based on one-tailed Wilcoxon rank-sum test with Bonferroni correction for multiple comparisons. Two sets of pairs were evaluated: controls versus ablation conditions (top) and PR2/3 double-ablated animals versus PR2 and PR3 single-ablated animals (bottom) (*$p < 0.05$; **$p < 0.01$; ***$p < 0.001$; no asterisk, $p > 0.05$; full statistics in Table S3A).

(D and E) Schematic (D) and photograph (E) of outdoor-optomotor arena (STAR Methods).

(F) Average position of all fish per side over time; dotted lines illustrate control-like performance.

(G) Quantification of mean optomotor performance per condition in (F) (*$p < 0.05$; ***$p < 0.001$; no asterisk, $p > 0.05$; full statistics in Table S3B).

(H and I) Quantification of mean optomotor performance per additional batch of control and PR2/3 double-ablated animals (H) and their heterogeneity across experiments (I), cf. Figure S7.

(J) Spectral dependence of phototaxis behavior in controls (gray), with power-adjusted spectral tuning of melanopsin superimposed, assuming peak absorption (λ_{max}) at 480 nm.

(K) Corresponding spectral dependences of phototaxis behavior following cone ablations. For simplicity, only medians and interquartile ranges are shown; dotted line indicates control-like performance. Statistics of spectral positions against controls based on one-tailed Wilcoxon rank-sum tests with Bonferroni correction for multiple comparisons (*$p < 0.05$; **$p < 0.01$; ***$p < 0.001$; no asterisk, $p > 0.05$; full statistics in Table S3C).

See also Figures S6 and S7.

Please cite this article in press as: Fornetto et al., Zebrafish use spectral information to suppress the visual background, Cell (2025), https://doi.org/10.1016/j.cell.2025.10.009

exhibited robust and highly statistically significant defects in optomotor behavior relative to controls. By contrast, PR2-, PR3-, and PR2/3-ablated animals exhibited no significant defects. In fact, PR3-ablated animals weakly but significantly outperformed controls.

PR2/3 double ablation reduces optomotor variability

Beyond their matched mean optomotor performance, PR2/3 double-ablated animals also appeared to exhibit less-variable optomotor responses compared with controls (Figure 6G). To explore this possible effect, we recorded additional experiments under a variety of weather and water conditions (STAR Methods; Figure S7) and compared their mean performance (Figure 6H) and behavioral heterogeneity (Figure 6I). PR2/3 double-ablated animals and controls both continued to exhibit robust and statistically indistinguishable optomotor performance (Figure 6H), both when the same animals were tested repeatedly in close succession (Figure S7D, top) and when comparing across different animal batches, experimental days, and water conditions (Figure S7D, bottom, and Figures S7A–S7C and S7E–S7G; STAR Methods). Despite this, PR2/3 double-ablated animals behaved in a significantly more internally consistent manner compared with controls (Figure 6I). This reduced behavioral variability following the loss of PR2/3—apparently without a deterioration in overall performance—strikingly echoes their correspondingly reduced heterogeneity at the level of brain responses to spatiotemporally patterned stimuli (Figure 4G).

Cone regulation extends to intrinsically photosensitive circuits

Beyond rods (PR0)[22] and cones (PR1-n), vertebrate eyes also comprise intrinsically photosensitive circuits[44] that mostly serve "non-image-forming" visual functions, including the control of phototaxis.[32] This ancestral and probably universal behavior allows animals to use information about the intensity and spectrum of light to seek out optimal places in their environment.[45] In larval zebrafish, experimental ablation of intrinsically photosensitive retinal ganglion cells (ipRGCs) disrupts this behavior.[32] Nevertheless, ipRGCs cells do receive upstream synaptic inputs[44] and might therefore be subject to the same types of cone-regulatory influences that also impinge on PR1/4-driven circuits.

To test this idea, we first determined the spectral dependence of phototactic behavior in controls. Melanopsin, the photopigment expressed in ipRGCs, is green/blue sensitive (λ_{max} ~480 nm),[44] so in the absence of additional inputs from cones, phototaxis should be best driven by mid-wavelength light. However, this was not the case. Instead, phototaxis was spectrally biphasic and was best driven by UV or red light (Figure 6J; Video S4). We therefore next ablated different cones to probe which types contribute to phototactic behavior and how (Figure 6K).

First, PR4 ablation led to highly significant reductions in phototactic performance, including at long wavelengths where PR4 is insensitive. Accordingly, while the loss of the UV response points at a direct role of PR4 in driving phototaxis, the more general loss of responsiveness across all wavelengths rather argues for an effect on behavioral state. Second, PR1 ablation had no significant effect on phototaxis. This indicates that it is possible, in principle, to robustly drive "basic" visual behavior without the use of PR1, despite its apparently indispensable role in spatiotemporal vision (Figures 1, 2, 3, 4, 5 and 6A–6I). Third, PR2 ablation strongly accentuated phototactic behavior and, moreover, shifted the overall spectral tuning to more closely align with a potential joint drive from PR4 and melanopsin alone. This implies that PR2 normally suppresses phototactic behavior. Fourth, and opposite to PR2, PR3 ablation reduced phototactic performance. Accordingly, PR2 and PR3 cone circuits again acted in mutual opposition. However, importantly, in the case of phototaxis, the roles of PR2 versus PR3 were inverted, with PR2 providing the principal suppression and PR3 counteracting this effect. Finally, as already observed for both spontaneous swimming (Figure 5D) and optomotor performance (Figure 6C), concurrent ablation of both PR2 and PR3 again rescued both PR2 and PR3 single-ablation phenotypes to near-control levels (Figure 6K).

DISCUSSION

An alternative view on the organization of cone circuits for aquatic vision

Our results challenge the "classical view" on the ancestrally aquatic functional organization of cone circuits in the vertebrate retina (Figure 7A). In this view, visuo-behavioral circuits are dominated by grayscale signals that emerge from a weighted sum across cones.[23,46] Antagonistic cone contributions, where present, are solely attributed to color vision.[14,46]

However, this view cannot explain (1) the complete loss of responses to the tested spatiotemporal patterns following the ablation of PR1 and PR4 (Figures 2 and 3), as PR2 and PR3 cones should continue to drive relatively normal vision in their absence; (2) the widespread white bias of zebrafish vision (Figure 1), the loss of this bias following the ablation of PR2/3 (Figures 4A–4F), or the concurrent accentuation of spatiotemporal pattern responses (Figures 2 and 3), as explaining any of these results requires a net-negative contribution of PR2 and PR3 to vision; and (3) the "rescuing" of PR2 and PR3 single-ablation phenotypes upon the concurrent ablation of both cones (brain functions: Figures 2, 3, and 4; behaviors: Figures 5 and 6) because, in the classical view, ablating cones cannot improve performance.

Instead, our results strongly support an alternative model[9] of the functional organization of cone circuits in the zebrafish retina (Figure 7B). Herein, vision is primarily driven by weighted contributions from PR1 and PR4 alone. PR0 (rods), which are not yet mature in larval zebrafish,[47] probably extend this principal drive to low-light conditions.[9] Intrinsically photosensitive circuits add further drive to a subset of circuits. Together, these four photoreceptor systems may form the ancestral core of vision, and for normal function, their concurrent presence is probably non-optional. In agreement, nearly all extant vertebrates, including humans, retain all four systems in their eyes.[9,18,22,27]

Conversely, in zebrafish at least, PR2 and PR3 do not drive vision. Instead, they form an auxiliary system tasked with regulating the core circuits. Within auxiliary circuits, PR2 and PR3 interact in mutual opposition, and the net result of this interaction, including its sign, dictates the nature of the regulatory input to different core circuits (Figure 7C). For zebrafish vision, the

Please cite this article in press as: Fornetto et al., Zebrafish use spectral information to suppress the visual background, Cell (2025), https://doi.org/10.1016/j.cell.2025.10.009

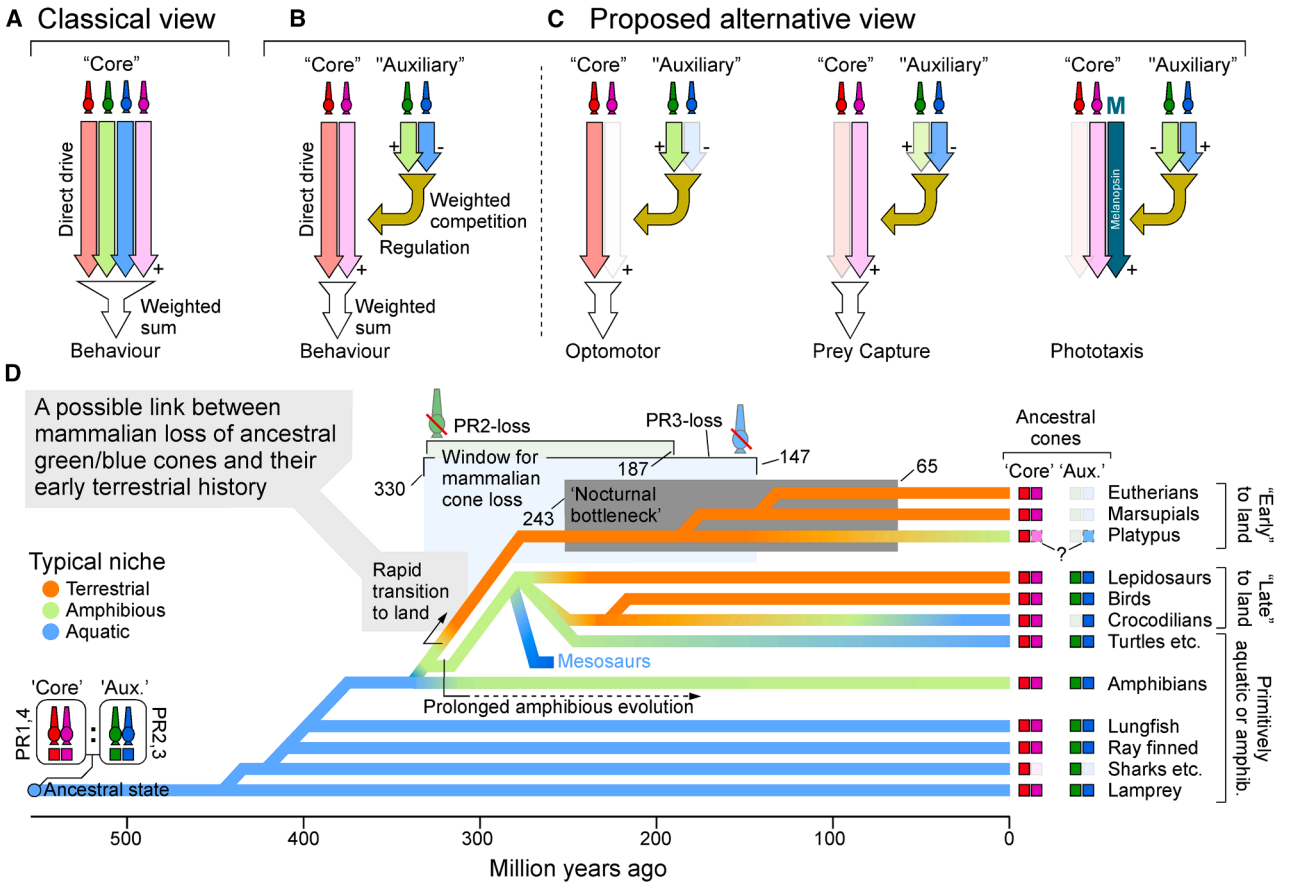

Figure 7. An alternative view on the organization of cone circuits for vertebrate vision

(A) Classical view of cone signal cooperating to jointly drive behavioral circuits.

(B) Proposed alternative circuit architecture, where PR1 and PR4 alone represent retinal core circuits that jointly drive all visual behavior. By contrast, PR2 and PR3 circuits form an auxiliary circuit that acts in mutual opposition to suppress, and thereby regulate, the core drive.

(C) Suggested weight adjustment within this architecture for different subsets of visuo-behavioral circuits.

(D) Approximate phylogenetic history of extant vertebrates with inferred ancestral patterns of territorialization coded in color, from aquatic beginnings (blue) via amphibious lifestyles (green) to full terrestrialization (orange). Terrestrialization probably occurred rapidly in the lineage that led to modern-day mammals, but more gradually so in the lineage that led to modern-day reptiles, including birds. This pattern correlates with the widespread retention of the ancestral auxiliary cones in most non-mammalian tetrapods and, conversely, their systematic loss in probably all mammals (for platypus, see Discussion). For references, see main text.

presence of PR2 and/or PR3 for robust vision is probably inessential, putatively in line with the profusion of vertebrate lineages—including humans—that have independently lost them.[9,18,22]

Auxiliary cone circuits may represent an aquatic trait

We have shown that, in zebrafish, one central role of the PR2/3 auxiliary cone system is to spectrally suppress visual responses to the background. However, this "foreground trick" cannot work on land due to the greatly reduced scattering and absorption of light in air.[48] For terrestrial vision, the same net-suppressive cone architecture would likely limit the signal-to-noise ratio of the visual system without conferring benefits to distance estimation. Correspondingly, it seems reasonable to suggest that the functional architecture of auxiliary cone circuits, as found in zebrafish, represents an adaptation for aquatic vision, the ancestral remit of the vertebrate eye.[9,24,48]

If so, we should consider the possibility that the systematic loss of auxiliary cones in mammals—but not in birds, reptiles, or amphibians[9,18]—may link with differences in the speed by which their early ancestors transitioned from the water to land[25,49] (Figure 7D). Most amphibians remain closely associated with the water to the present day, and the ancestors of reptiles and birds likely remained semi-aquatic for millions of years following their first emergence on land. This slow transition to land could have offered an opportunity to gradually modify the originally aquatic retinal architecture for terrestrial vision. By contrast, soon after their divergence from other amniotes, the ancestors of mammals rapidly transitioned to land, and, perhaps along with it, the auxiliary cone system was lost.

Revisiting Walls' nocturnal bottleneck theory

Contrasting the foregoing, Walls' classic theory[26] links mammalian cone loss to nocturnality during the dinosaur age

Please cite this article in press as: Fornetto et al., Zebrafish use spectral information to suppress the visual background, Cell (2025), https://doi.org/10.1016/j.cell.2025.10.009

(~240–65 mya), arguing that PR2 and PR3—assumed to serve color vision—conferred little advantage across ~175 million years of night activity. However, this view deserves re-examination.

First, the idea that cone loss reflected a lack of spectral information at night is doubtful: nocturnal skylight resembles daylight spectrally,[50] and many non-mammalian vertebrates[51–53] and invertebrates[54] achieve nocturnal color vision via enhanced receptor sensitivity. Second, our data indicate that functions beyond color vision may underlie PR2/3 loss. In zebrafish, PR2/3 aid underwater foreground enhancement, but other non-color roles likely exist. Third, PR2/3 loss may have preceded mammals' "nocturnal bottleneck." PR2 is absent in all mammals[22,48,55] and may therefore have disappeared soon after their lineage's divergence from sauropsida (~318 mya). PR3 is also absent, except possibly in platypus, which retain the PR3 opsin gene SWS2 and PR3 transcription factor FOXQ2.[22,56] However, opsin identity is an incomplete predictor of cone type,[22] and FOXQ2 has functions beyond the retina.[57] Moreover, unusual for small mammals,[9,17] platypus lack the ancestral PR4 opsin SWS1, raising the possibility that they express SWS2 opsin in PR4. If so, mammalian PR3 loss may also predate dinosaurs; otherwise, and arguably in further conflict with Walls' theory, PR3 must have persisted through ~50 million years of nocturnality in stem mammals until the divergence of monotremes and marsupials (~187–210 mya) and the entire bottleneck in the platypus lineage.

Possible circuitry underlying net-suppressive wiring of the green/blue system

The net-suppressive action of PR2 and PR3 circuits could be plausibly explained by established retinal organization.[9,16,23,41,58] Horizontal cells set initial cone opponencies,[15] while bipolar cells pool signals from neighboring cones in type-specific ways,[59] thereby producing parallel on and off pathways.[58] As a population, bipolar cells therefore generate systematic mixtures of cone signals in two polarities, mapped onto fixed depths of the inner retina,[30,41,60] creating "spectral layering."[9] In fish[60] and other non-mammals,[61–64] multistratified bipolar cells let on and off signals coexist within the same retinal layers. Together, this anatomical arrangement allows cone mixtures to map flexibly onto behaviors.[9,48] For instance, zebrafish ganglion cells for motion stratify in outer layers, while those for prey capture stratify centrally.[9,34,37,65] Aspects of such spectral[66,67] and behavioural[68] layering are conserved in mammals.[68] Together, in zebrafish, the systematic inner retinal mapping of different cone mixtures provides a simple and flexible bridge from cones to behavior. In support of this, the retinal output to the brain of fish,[69] birds,[70] reptiles,[63,71] and amphibians,[57] but not mammals,[68] is dominated by on-off circuits.[29] Any "missing" cone mixtures, including presumably important balancing contributions, can then be provided by amacrine cells.[60,72,73] Beyond the retina, central circuits may establish additional cone contrasts,[13,31,74] for example, within the extensive inhibitory plexus of the retinorecipient (pre)tectum.[75,76]

Limitations of the study

Despite the ancestral nature of PR1–4 cones, it remains unclear whether and how other vertebrate species, including both aquatic and terrestrial ones, use their diverse cone complements in ways that align with insights gained from larval zebrafish. It also remains unclear how our findings translate to vision in adult zebrafish. Likewise, whether and how the zebrafish cones differentially wire into downstream circuitries to support their differential roles in vision remains incompletely understood. Here, it will also be key to address how the circuit mechanism that leads to the here-described "whitening" effect relates to those used for "perceptual" color vision in zebrafish[16] and beyond.[48,77,78]

RESOURCE AVAILABILITY

Lead contact

Requests for further information and resources should be directed to, and will be fulfilled by, the lead contact, Tom Baden (t.baden@sussex.ac.uk).

Materials availability

Plasmid pTol2-elavl3-H2B-GCaMP6s used in this study has been deposited in Addgene (Plasmid #59530). The transgenic lines used in this study are available upon request to the lead author.

Data and code availability

- All data reported in this paper will be shared by the lead contact upon request.
- This paper does not report original code.
- Any additional information required to reanalyze the data reported in this paper is available from the lead contact upon request.

ACKNOWLEDGMENTS

We thank Takeshi Yoshimatsu for providing the original single-cone-ablation lines, including the previously unpublished PR2 ablation line; Patricio Simoes and Leon Lagnado for access to their OMR setup; and Emma Alexander for providing the underwater video used in Video S1. We also thank Michel Laurin for key discussions around vertebrates' aquatic histories and Leon Lagnado for critical feedback on a draft of the manuscript. Funding was provided by the Wellcome Trust (Investigator Award in Science 220277/Z20/Z), the European Research Council (ERC-StG "NeuroVisEco" 677687 and ERC-AdG "Cones4Action," covered under the UK's EPSRC guarantee scheme EP/Z533981/1), UKRI (BBSRC, BB/R014817/1, and BB/W013509/1), the Leverhulme Trust (PLP-2017-005, RPG-2021-026, and RPG-2-23-042), and the Lister Institute for Preventive Medicine. This research was funded in part by the Wellcome Trust (220277/Z20/Z). To promote Open Access, the authors have applied a CC BY public copyright license to any author accepted manuscript version arising from this submission.

AUTHOR CONTRIBUTIONS

Conceptualization, C.F. and T.B.; design, C.F. and T.B.; data collection, C.F.; data processing, C.F. and T.B.; modeling, T.B.; materials, C.F. and T.E.; supervision, T.B.; writing – original draft, T.B.; writing – review & editing, T.B., C.F., and T.E.; funding, T.B. and T.E.

DECLARATION OF INTERESTS

The authors declare no competing interests.

DECLARATION OF GENERATIVE AI AND AI-ASSISTED TECHNOLOGIES IN THE WRITING PROCESS

During the preparation of this work, the author(s) used ChatGPT 5 to shorten and/or streamline parts of the text. After using this tool/service, the author(s) reviewed and edited the content as needed and take(s) full responsibility for the content of the publication.

STAR★METHODS

Detailed methods are provided in the online version of this paper and include the following:

- KEY RESOURCES TABLE
- EXPERIMENTAL MODEL AND STUDY PARTICIPANT DETAILS
  - Animals
- METHOD DETAILS
  - Two-photon calcium imaging and visual stimulation
  - QDSpy
  - Two-photon data analysis
  - Cone ablations
  - DNA extraction and genotyping
  - Indoor Optomotor assay and spontaneous swimming
  - Outdoor optomotor assay
  - Phototaxis
  - Natural scene processing
  - Modelling of cone drive
- QUANTIFICATION AND STATISTICAL ANALYSIS

SUPPLEMENTAL INFORMATION

Supplemental information can be found online at https://doi.org/10.1016/j.cell.2025.10.009.

Received: April 17, 2025
Revised: August 18, 2025
Accepted: October 6, 2025

REFERENCES

1. Nilsson, D.-E. (2021). The Diversity of Eyes and Vision. Annu. Rev. Vis. Sci. *7*, 19–41. https://doi.org/10.1146/annurev-vision-121820-074736.
2. Hsiang, J.C., Johnson, K.P., Madisen, L., Zeng, H., and Kerschensteiner, D. (2017). Local processing in neurites of VGluT3-expressing amacrine cells differentially organizes visual information. eLife *6*, e31307. https://doi.org/10.7554/eLife.31307.
3. Zhang, Y., Kim, I.-J., Sanes, J.R., and Meister, M. (2012). The most numerous ganglion cell type of the mouse retina is a selective feature detector. Proc. Natl. Acad. Sci. USA. *109*, E2391–E2398. https://doi.org/10.1073/pnas.1211547109.
4. Masland, R.H. (2012). The tasks of amacrine cells. Vis. Neurosci. *29*, 3–9. https://doi.org/10.1017/s0952523811000344.
5. Strauss, S., Korympidou, M.M., Ran, Y., Franke, K., Schubert, T., Baden, T., Berens, P., Euler, T., and Vlasits, A.L. (2022). Center-surround interactions underlie bipolar cell motion sensing in the mouse retina. Nat. Commun. *13*, 5574. https://doi.org/10.1038/s41467-022-32762-7.
6. Johnson, K.P., Fitzpatrick, M.J., Zhao, L., Wang, B., McCracken, S., Williams, P.R., and Kerschensteiner, D. (2021). Cell-type-specific binocular vision guides predation in mice. Neuron *109*, 1527–1539.e4. https://doi.org/10.1016/j.neuron.2021.03.010.
7. Nityananda, V., and Read, J.C.A. (2017). Stereopsis in animals: evolution, function and mechanisms. J. Exp. Biol. *220*, 2502–2512. https://doi.org/10.1242/jeb.143883.
8. Yonas, A., Elieff, C.A., and Arterberry, M.E. (2002). Emergence of sensitivity to pictorial depth cues: Charting development in individual infants. Infant Behav. Dev. *25*, 495–514. https://doi.org/10.1016/S0163-6383(02)00147-9.
9. Baden, T. (2024). Ancestral photoreceptor diversity as the basis of visual behaviour. Nat. Ecol. Evol. *8*, 374–386. https://doi.org/10.1038/s41559-023-02291-7.
10. Janiak, F.K., Bartel, P., Bale, M.R., Yoshimatsu, T., Komulainen, E., Zhou, M., Staras, K., Prieto-Godino, L.L., Euler, T., Maravall, M., et al. (2022). Non-telecentric two-photon microscopy for 3D random access mesoscale imaging. Nat. Commun. *13*, 544. https://doi.org/10.1038/s41467-022-28192-0.
11. Franke, K., Maia Chagas, A.M., Zhao, Z., Zimmermann, M.J.Y.Y., Bartel, P., Qiu, Y., Szatko, K.P., Baden, T., and Euler, T. (2019). An arbitrary-spectrum spatial visual stimulator for vision research. eLife *8*, e48779. https://doi.org/10.7554/eLife.48779.
12. Wozniak, B., and Dera, J. (2006). Light Absorption in Sea Water (Springer) https://doi.org/10.1007/978-0-387-49560-6.
13. Bartel, P., Janiak, F.K., Osorio, D., and Baden, T. (2021). Colourfulness as a possible measure of object proximity in the larval zebrafish brain. Curr. Biol. *31*, R235–R236. https://doi.org/10.1016/j.cub.2021.01.030.
14. Baden, T., and Osorio, D. (2019). The Retinal Basis of Vertebrate Color Vision. Annu. Rev. Vis. Sci. *5*, 177–200. https://doi.org/10.1146/annurev-vision-091718-014926.
15. Yoshimatsu, T., Bartel, P., Schröder, C., Janiak, F.K., St-Pierre, F., Berens, P., and Baden, T. (2021). Ancestral circuits for vertebrate color vision emerge at the first retinal synapse. Sci. Adv. *7*, eabj6815. https://doi.org/10.1126/SCIADV.ABJ6815.
16. Baden, T. (2021). Circuit mechanisms for colour vision in zebrafish. Curr. Biol. *31*, R807–R820. https://doi.org/10.1016/j.cub.2021.04.053.
17. Hagen, J.F.D., Roberts, N.S., and Johnston, R.J. (2023). The evolutionary history and spectral tuning of vertebrate visual opsins. Dev. Biol. *493*, 40–66. https://doi.org/10.1016/j.ydbio.2022.10.014.
18. Tommasini, D., Yoshimatsu, T., Puthussery, T., Baden, T., and Shekhar, K. (2025). Comparative transcriptomic insights into the evolution of vertebrate photoreceptor types. Curr. Biol. *35*, 2228–2239.e4. https://doi.org/10.1016/j.cub.2025.03.060.
19. Liu, Y., Hurley, E.C., Ogawa, Y., Gause, M., Toomey, M.B., Myers, C.A., and Corbo, J.C. (2025). Avian photoreceptor homologies and the origin of double cones. Curr. Biol. *35*, 2215–2227.e6. https://doi.org/10.1016/j.cub.2025.02.040.
20. Wang, J., Zhang, L., Cavallini, M., Pahlevan, A., Sun, J., Morshedian, A., Fain, G.L., Sampath, A.P., and Peng, Y.-R. (2024). Molecular characterization of the sea lamprey retina illuminates the evolutionary origin of retinal cell types. Nat. Commun. *15*, 10761. https://doi.org/10.1038/s41467-024-55019-x.
21. Warrington, R.E., Davies, W.I.L., Hemmi, J.M., Hart, N.S., Potter, I.C., Collin, S.P., and Hunt, D.M. (2021). Visual opsin expression and morphological characterization of retinal photoreceptors in the pouched lamprey (Geotria australis, Gray). J. Comp. Neurol. *529*, 2265–2282. https://doi.org/10.1002/cne.25092.
22. Baden, T., Angueyra, J.M., Bosten, J.M., Collin, S.P., Conway, B.R., Cortesi, F., Dedek, K., Euler, T., Novales Flamarique, I.N., Franklin, A., et al. (2025). A standardized nomenclature for the rods and cones of the vertebrate retina. PLoS Biol. *23*, e3003157. https://doi.org/10.1371/journal.pbio.3003157.
23. Masland, R.H. (2001). The fundamental plan of the retina. Nat. Neurosci. *4*, 877–886. https://doi.org/10.1038/nn0901-877.
24. Kafetzis, G., Bok, M., Baden, T., and Nilsson, D.E. (2025). A median eye origin of the vertebrate retina explains its unique circuitry. Preprint at bioRxiv. https://doi.org/10.1101/2025.09.11.675609.
25. Laurin, M. (2010). How Vertebrates Left the Water (University of California Press).
26. Walls, G.L. (1942). The Vertebrate Eye and Its Adaptive Radiation (Cranbrook Institute of Science) https://doi.org/10.5962/bhl.title.7369.
27. Hahn, J., Monavarfeshani, A., Qiao, M., Kao, A.H., Kölsch, Y., Kumar, A., Kunze, V.P., Rasys, A.M., Richardson, R., Wekselblatt, J.B., et al. (2023). Evolution of neuronal cell classes and types in the vertebrate retina. Nature *624*, 415–424. https://doi.org/10.1038/s41586-023-06638-9.
28. Baden, T., Euler, T., and Berens, P. (2020). Understanding the retinal basis of vision across species. Nat. Rev. Neurosci. *21*, 5–20. https://doi.org/10.1038/s41583-019-0242-1.

29. Baden, T. (2024). The vertebrate retina: a window into the evolution of computation in the brain. Curr. Opin. Behav. Sci. *57*, 101391. https://doi.org/10.1016/j.cobeha.2024.101391.

30. Zimmermann, M.J.Y., Nevala, N.E., Yoshimatsu, T., Osorio, D., Nilsson, D.-E., Berens, P., and Baden, T. (2018). Zebrafish Differentially Process Color across Visual Space to Match Natural Scenes. Curr. Biol. *28*, 2018–2032.e5. https://doi.org/10.1016/j.cub.2018.04.075.

31. Guggiana-Nilo, D.A., and Engert, F. (2016). Properties of the Visible Light Phototaxis and UV Avoidance Behaviors in the Larval Zebrafish. Front. Behav. Neurosci. *10*, 160. https://doi.org/10.3389/fnbeh.2016.00160.

32. Kölsch, Y., Hahn, J., Sappington, A., Stemmer, M., Fernandes, A.M., Helmbrecht, T.O., Lele, S., Butrus, S., Laurell, E., Arnold-Ammer, I., et al. (2021). Molecular classification of zebrafish retinal ganglion cells links genes to cell types to behavior. Neuron *109*, 645–662.e9. https://doi.org/10.1016/j.neuron.2020.12.003.

33. Orger, M.B. (2016). The Cellular Organization of Zebrafish Visuomotor Circuits. Curr. Biol. *26*, R377–R385. https://doi.org/10.1016/j.cub.2016.03.054.

34. Matsuda, K., and Kubo, F. (2021). Circuit Organization Underlying Optic Flow Processing in Zebrafish. Front. Neural Circuits *15*, 709048. https://doi.org/10.3389/fncir.2021.709048.

35. Yoshimatsu, T., Schröder, C., Nevala, N.E., Berens, P., and Baden, T. (2020). Fovea-like Photoreceptor Specializations Underlie Single UV Cone Driven Prey-Capture Behavior in Zebrafish. Neuron *107*, 320–337.e6. https://doi.org/10.1016/j.neuron.2020.04.021.

36. Bianco, I.H., Kampff, A.R., and Engert, F. (2011). Prey Capture Behavior Evoked by Simple Visual Stimuli in Larval Zebrafish. Front. Syst. Neurosci. *5*, 101. https://doi.org/10.3389/fnsys.2011.00101.

37. Semmelhack, J.L., Donovan, J.C., Thiele, T.R., Kuehn, E., Laurell, E., and Baier, H. (2014). A dedicated visual pathway for prey detection in larval zebrafish. eLife *3*, e04878. https://doi.org/10.7554/eLife.04878.

38. Khan, B., Jaesiri, O.M., Lazarte, I.P., Li, Y., Tian, G., Zhao, P., Zhao, Y., Ho, V.D., and Semmelhack, J.L. (2023). Zebrafish larvae use stimulus intensity and contrast to estimate distance to prey. Curr. Biol. *33*, 3179–3191.e4. https://doi.org/10.1016/j.cub.2023.06.046.

39. Yoshimatsu, T., D'Orazi, F.D., Gamlin, C.R., Suzuki, S.C., Suli, A., Kimelman, D., Raible, D.W., and Wong, R.O. (2016). Presynaptic partner selection during retinal circuit reassembly varies with timing of neuronal regeneration in vivo. Nat. Commun. *7*, 10590. https://doi.org/10.1038/ncomms10590.

40. Curado, S., Stainier, D.Y.R., and Anderson, R.M. (2008). Nitroreductase-mediated cell/tissue ablation in zebrafish: a spatially and temporally controlled ablation method with applications in developmental and regeneration studies. Nat. Protoc. *3*, 948–954. https://doi.org/10.1038/nprot.2008.58.

41. Bartel, P., Yoshimatsu, T., Janiak, F.K., and Baden, T. (2021). Spectral inference reveals principal cone-integration rules of the zebrafish inner retina. Curr. Biol. *31*, 5214–5226.e4. https://doi.org/10.1016/j.cub.2021.09.047.

42. MacPhail, R.C., Brooks, J., Hunter, D.L., Padnos, B., Irons, T.D., and Padilla, S. (2009). Locomotion in larval zebrafish: Influence of time of day, lighting and ethanol. NeuroToxicology *30*, 52–58. https://doi.org/10.1016/j.neuro.2008.09.011.

43. Naumann, E.A., Fitzgerald, J.E., Dunn, T.W., Rihel, J., Sompolinsky, H., and Engert, F. (2016). From Whole-Brain Data to Functional Circuit Models: The Zebrafish Optomotor Response. Cell *167*, 947–960.e20. https://doi.org/10.1016/j.cell.2016.10.019.

44. Do, M.T.H. (2019). MELANOPSIN AND THE INTRINSICALLY PHOTOSENSITIVE RETINAL GANGLION CELLS: BIOPHYSICS TO BEHAVIOR. Neuron *104*, 205–226. https://doi.org/10.1016/j.neuron.2019.07.016.

45. Jékely, G. (2009). Evolution of phototaxis. Philos. Trans. R. Soc. Lond. B Biol. Sci. *364*, 2795–2808. https://doi.org/10.1098/rstb.2009.0072.

46. Buchsbaum, G., and Gottschalk, A. (1983). Trichromacy, opponent colours coding and optimum colour information transmission in the retina. Pap. R. Soc. Lond. B. Biol. Sci *220*, 89–113. https://doi.org/10.1098/rspb.1983.0090.

47. Fadool, J.M. (2003). Development of a rod photoreceptor mosaic revealed in transgenic zebrafish. Dev. Biol. *258*, 277–290. https://doi.org/10.1016/S0012-1606(03)00125-8.

48. Baden, T. (2024). From water to land: Evolution of photoreceptor circuits for vision in air. PLoS Biol. *22*, e3002422. https://doi.org/10.1371/journal.pbio.3002422.

49. Laurin, M., and de Buffrénil, V. (2016). Microstructural features of the femur in early ophiacodontids: A reappraisal of ancestral habitat use and lifestyle of amniotes. C. R. Palevol *15*, 115–127. https://doi.org/10.1016/j.crpv.2015.01.001.

50. Nilsson, D.-E., and Smolka, J. (2021). Quantifying biologically essential aspects of environmental light. J. R. Soc. Interface *18*, 20210184. https://doi.org/10.1098/rsif.2021.0184.

51. Donner, K., and Yovanovich, C.A.M. (2020). A frog's eye view: Foundational revelations and future promises. Semin. Cell Dev. Biol. *106*, 72–85. https://doi.org/10.1016/j.semcdb.2020.05.011.

52. Rozenblit, F., and Gollisch, T. (2020). What the salamander eye has been telling the vision scientist's brain. Semin. Cell Dev. Biol. *106*, 61–71. https://doi.org/10.1016/j.semcdb.2020.04.010.

53. Kojima, K., Matsutani, Y., Yanagawa, M., Imamoto, Y., Yamano, Y., Wada, A., Shichida, Y., and Yamashita, T. (2021). Evolutionary adaptation of visual pigments in geckos for their photic environment. Sci. Adv. *7*, eabj1316. https://doi.org/10.1126/sciadv.abj1316.

54. Warrant, E., and Somanathan, H. (2022). Colour vision in nocturnal insects. Philos. Trans. R. Soc. Lond. B Biol. Sci. *377*, 20210285. https://doi.org/10.1098/rstb.2021.0285.

55. Jacobs, G.H. (2009). Evolution of colour vision in mammals. Philos. Trans. R. Soc. Lond. B Biol. Sci. *364*, 2957–2967. https://doi.org/10.1098/rstb.2009.0039.

56. Ogawa, Y., Shiraki, T., Fukada, Y., and Kojima, D. (2021). Foxq2 determines blue cone identity in zebrafish. Sci. Adv. *7*, eabi9784. https://doi.org/10.1126/sciadv.abi9784.

57. Dai, Y., Zhong, Y., Pan, R., Yuan, L., Fu, Y., Chen, Y., Du, J., Li, M., Wang, X., Liu, H., et al. (2024). Evolutionary origin of the chordate nervous system revealed by amphioxus developmental trajectories. Nat. Ecol. Evol. *8*, 1693–1710. https://doi.org/10.1038/s41559-024-02469-7.

58. Euler, T., Haverkamp, S., Schubert, T., and Baden, T. (2014). Retinal Bipolar Cells: Elementary Building Blocks of Vision. Nat. Rev. Neurosci. *15*, 507–519. https://doi.org/10.1038/nrn3783.

59. Li, Y.N., Tsujimura, T., Kawamura, S., and Dowling, J.E. (2012). Bipolar cell-photoreceptor connectivity in the zebrafish (Danio rerio) retina. J. Comp. Neurol. *520*, 3786–3802. https://doi.org/10.1002/cne.23168.

60. Wang, X., Roberts, P.A., Yoshimatsu, T., Lagnado, L., and Baden, T. (2023). Amacrine cells differentially balance zebrafish color circuits in the central and peripheral retina. Cell Rep. *42*, 112055. https://doi.org/10.1016/j.celrep.2023.112055.

61. Günther, A., Dedek, K., Haverkamp, S., Irsen, S., Briggman, K.L., and Mouritsen, H. (2021). Double cones and the diverse connectivity of photoreceptors and bipolar cells in an avian retina. J. Neurosci. *41*, 5015–5028. https://doi.org/10.1523/JNEUROSCI.2495-20.2021.

62. Seifert, M., Baden, T., and Osorio, D. (2020). The retinal basis of vision in chicken. Semin. Cell Dev. Biol. *106*, 106–115. https://doi.org/10.1016/j.semcdb.2020.03.011.

63. Ammermüller, J., and Kolb, H. (1995). The organization of the turtle inner retina. I. ON- and OFF-center pathways. J. Comp. Neurol. *358*, 1–34. https://doi.org/10.1002/cne.903580102.

64. Wu, S.M., Gao, F., and Maple, B.R. (2000). Functional Architecture of Synapses in the Inner Retina: Segregation of Visual Signals by Stratification of

Bipolar Cell Axon Terminals. J. Neurosci. *20*, 4462–4470. https://doi.org/10.1523/JNEUROSCI.20-12-04462.2000.

65. Robles, E., Laurell, E., and Baier, H. (2014). The Retinal Projectome Reveals Brain-Area-Specific Visual Representations Generated by Ganglion Cell Diversity. Curr. Biol. *24*, 2085–2096. https://doi.org/10.1016/j.cub.2014.07.080.
66. Behrens, C., Schubert, T., Haverkamp, S., Euler, T., and Berens, P. (2016). Connectivity map of bipolar cells and photoreceptors in the mouse retina. eLife *5*, e20041. https://doi.org/10.7554/eLife.20041.
67. Szatko, K.P., Korympidou, M.M., Ran, Y., Berens, P., Dalkara, D., Schubert, T., Euler, T., and Franke, K. (2020). Neural circuits in the mouse retina support color vision in the upper visual field. Nat. Commun. *11*, 3481. https://doi.org/10.1038/s41467-020-17113-8.
68. Goetz, J., Jessen, Z.F., Jacobi, A., Mani, A., Cooler, S., Greer, D., Kadri, S., Segal, J., Shekhar, K., Sanes, J.R., et al. (2022). Unified classification of mouse retinal ganglion cells using function, morphology, and gene expression. Cell Rep. *40*, 111040. https://doi.org/10.1016/j.celrep.2022.111040.
69. Zhou, M., Bear, J., Roberts, P.A., Janiak, F.K., Semmelhack, J., Yoshimatsu, T., and Baden, T. (2020). Zebrafish Retinal Ganglion Cells Asymmetrically Encode Spectral and Temporal Information across Visual Space. Curr. Biol. *30*, 2927–2942.e7. https://doi.org/10.1016/j.cub.2020.05.055.
70. Seifert, M., Roberts, P.A., Kafetzis, G., Osorio, D., and Baden, T. (2023). Birds multiplex spectral and temporal visual information via retinal On- and Off-channels. Nat. Commun. *14*, 5308. https://doi.org/10.1038/s41467-023-41032-z.
71. Ammermüller, J., Muller, J.F., and Kolb, H. (1995). The organization of the turtle inner retina. II. Analysis of color-coded and directionally selective cells. J. Comp. Neurol. *358*, 35–62. https://doi.org/10.1002/cne.903580103.
72. Torvund, M.M., Ma, T.S., Connaughton, V.P., Ono, F., and Nelson, R.F. (2017). Cone signals in monostratified and bistratified amacrine cells of adult zebrafish retina. J. Comp. Neurol. *525*, 1532–1557. https://doi.org/10.1002/cne.24107.
73. Korympidou, M.M., Strauss, S., Schubert, T., Franke, K., Berens, P., Euler, T., and Vlasits, A.L. (2024). GABAergic amacrine cells balance biased chromatic information in the mouse retina. Cell Rep. *43*, 114953. https://doi.org/10.1016/j.celrep.2024.114953.
74. Fornetto, C., Tiso, N., Pavone, F.S., and Vanzi, F. (2020). Colored visual stimuli evoke spectrally tuned neuronal responses across the central nervous system of zebrafish larvae. BMC Biol. *18*, 172. https://doi.org/10.1186/s12915-020-00903-3.
75. Sajovic, P., and Levinthal, C. (1983). Inhibitory mechanism in zebrafish optic tectum: Visual response properties of tectal cells altered by picrotoxin and bicuculline. Brain Res. *271*, 227–240. https://doi.org/10.1016/0006-8993(83)90285-8.
76. Petkova, M.D., Januszewski, M., Blakely, T., Herrera, K.J., Schuhknecht, G.F.P., Tiller, R., Choi, J., Schalek, R.L., Boulanger-Weill, J., Peleg, A., et al. (2025). A connectomic resource for neural cataloguing and circuit dissection of the larval zebrafish brain. Preprint at bioRxiv. https://doi.org/10.1101/2025.06.10.658982.
77. Bowmaker, J.K. (1998). Evolution of colour vision in vertebrates. Eye (Lond) *12*, 541–547. https://doi.org/10.1038/eye.1998.143.
78. Kelber, A. (2019). Bird colour vision – from cones to perception. Curr. Opin. Behav. Sci. *30*, 34–40. https://doi.org/10.1016/j.cobeha.2019.05.003.
79. Vladimirov, N., Mu, Y., Kawashima, T., Bennett, D.V., Yang, C.-T., Looger, L.L., Keller, P.J., Freeman, J., and Ahrens, M.B. (2014). Light-sheet functional imaging in fictively behaving zebrafish. Nat. Methods *11*, 883–884. https://doi.org/10.1038/nmeth.3040.
80. Salbreux, G., Barthel, L.K., Raymond, P.A., and Lubensky, D.K. (2012). Coupling Mechanical Deformations and Planar Cell Polarity to Create Regular Patterns in the Zebrafish Retina. PLoS Comput. Biol. *8*, e1002618. https://doi.org/10.1371/journal.pcbi.1002618.
81. Davison, J.M., Akitake, C.M., Goll, M.G., Rhee, J.M., Gosse, N., Baier, H., Halpern, M.E., Leach, S.D., and Parsons, M.J. (2007). Transactivation from Gal4-VP16 transgenic insertions for tissue-specific cell labeling and ablation in zebrafish. Dev. Biol. *304*, 811–824. https://doi.org/10.1016/j.ydbio.2007.01.033.
82. Guilbeault, N.C., Guerguiev, J., Martin, M., Tate, I., and Thiele, T.R. (2021). BonZeb: open-source, modular software tools for high-resolution zebrafish tracking and analysis. Sci. Rep. *11*, 8148. https://doi.org/10.1038/s41598-021-85896-x.
83. Lopes, G., Bonacchi, N., Frazão, J., Neto, J.P., Atallah, B.V., Soares, S., Moreira, L., Matias, S., Itskov, P.M., Correia, P.A., et al. (2015). Bonsai: an event-based framework for processing and controlling data streams. Front. Neuroinform. *9*, 7. https://doi.org/10.3389/fninf.2015.00007.
84. Baden, T., Berens, P., Franke, K., Román Rosón, M., Bethge, M., and Euler, T. (2016). The functional diversity of retinal ganglion cells in the mouse. Nature *529*, 345–350. https://doi.org/10.1038/nature16468.
85. Meeker, N.D., Hutchinson, S.A., Ho, L., and Trede, N.S. (2007). Method for Isolation of PCR-Ready Genomic DNA from Zebrafish Tissues. BioTechniques *43*, 610–614. https://doi.org/10.2144/000112619.
86. Wilkinson, R.N., Elworthy, S., Ingham, P.W., and van Eeden, F.J.M. (2013). A method for high-throughput PCR-based genotyping of larval zebrafish tail biopsies. BioTechniques *55*, 314–316. https://doi.org/10.2144/000114116.
87. Alexander, E., Cai, L.T., Fuchs, S., Hladnik, T.C., Zhang, Y., Subramanian, V., Guilbeault, N.C., Vijayakumar, C., Arunachalam, M., Juntti, S.A., et al. (2022). Optic flow in the natural habitats of zebrafish supports spatial biases in visual self-motion estimation. Curr. Biol. *32*, 5008–5021.e8. https://doi.org/10.1016/j.cub.2022.10.009.

Please cite this article in press as: Fornetto et al., Zebrafish use spectral information to suppress the visual background, Cell (2025), https://doi.org/10.1016/j.cell.2025.10.009

STAR★METHODS

KEY RESOURCES TABLE

REAGENT or RESOURCE	SOURCE	IDENTIFIER
Chemicals, peptides, and recombinant proteins		
1-phenyl-2-thiourea	Sigma-Aldrich	Cat# P7629
α-bungarotoxin	Tocris	Cat# 2133
Low gelling temperature agarose	Sigma-Aldrich	Cat# A9414
Tricaine	Sigma-Aldrich	Cat# A5040
NaOH	Sigma-Aldrich	Cat# 221465
Tris-HCl, pH 8.0	Thermo Fisher Scientific	Cat# 15568025
OneTaq Quick-Load 2X Master Mix	Biolabs	Cat# M0486S
Agarose	Meridian bioscience	Cat# BIO-41025
SYBR Safe DNA Gel Stain	Invitrogen	Cat# S33102
TAE Buffer	Thermo Fisher Scientific	Cat# B49
Low range DNA ladder	Meridian bioscience	Cat# BIO-33056
Metronidazole	Sigma-Aldrich	Cat# M3761
Experimental models: Organisms/strains		
Danio rerio (zebrafish): *Tg(elavl3:H2B-GCamP6s)*	Vladimirov et al.[79]	N/A
Tg(opn1sw1:nfsBmCherry)	Yoshimatsu et al.[39]	N/A
Tg(opn1sw2:nfsBmCherry)	Salbreux et al.[80]	N/A
Tg(trβ2:Gal4; UAS:nfsBmCherry)	Davison et al.[81]	N/A
Tg(LCR:nfsBmCherry)	This paper	N/A
Oligonucleotides		
Primers for genotyping:	N/A	N/A
sw1:nfsBmCherry: forward 5'-TCAAGAAACTCGTGAGGGGT-3' reverse 5'-TCAACAACCAGCTTCAGCCA-3'	This paper	N/A
sws2:nfsBmCherry: forward 5'-GCTGGTGACAACAAACCTCA reverse 5'- GTGCGAGGCATCAAGCATTT-3'	This paper	N/A
LCR:nfsBmCherry: forward 5'-GCAAATGTCCTAAATGAATTT GTGT-3' reverse 5'- ATAAAATGCCACGGCTGGGA-3'	This paper	N/A
trβ2:Gal4 UAS:nfsBmCherry: forward 5'- TGCGCCAAGTGTCT GAAGAA-3' reverse 5'- TCCGATGATGATGTCGCACT-3'	This paper	N/A
Recombinant DNA		
pTol2-elavl3-H2B-GCaMP6s	Vladimirov et al.[79]	RRID:Addgene_59530
pTol2-Sws1:nfsB-mCherry	Yoshimatsu et al.[39]	N/A
pTol2-Sws2:nfsB-mCherry	Salbreux et al.[80]	N/A
pTol2-CG2-trb2-Gal4; pTol2-UAS:nfsBmCherry	Davison et al.[81]	N/A
pTol2-LCR:nfsB-mCherry	This paper	N/A
Software and algorithms		
Igor Pro 9	Wavemetrics	https://www.wavemetrics.com/software/igor-pro-9
Matlab	Matlab R2021b	https://uk.mathworks.com/
Fiji	ImageJ	https://imagej.net/software/fiji/downloads
Bonsai – BonZeb package	Guilbeault et al.[82] and Lopes et al.[83]	https://bonsai-rx.org/
QDSpy	Franke et al.[11]	https://github.com/eulerlab/QDSpy

Please cite this article in press as: Fornetto et al., Zebrafish use spectral information to suppress the visual background, Cell (2025), https://doi.org/10.1016/j.cell.2025.10.009

CellPress
OPEN ACCESS

EXPERIMENTAL MODEL AND STUDY PARTICIPANT DETAILS

Animals

All procedures were performed in accordance with the U.K. Animals (Scientific Procedures) Act 1986 and approved by the animal welfare committee of the University of Sussex. Adults and larval zebrafish were maintained at 28°C on a 14:10 hour light:dark cycle. Embryos and larvae were raised in fish water. For all experiments, we used 6-8 days post fertilization (dpf) zebrafish (*Danio rerio*) larvae. For behavioural assays we used wild-type (AB) or *nacre* -/- zebrafish. The latter are mutants without pigments in the skin, but they retain wild-type eye pigmentation. For imaging recordings, 0.1 mM 1-phenyl-2-thiourea (PTU; Sigma-Aldrich, P7629) has been added to fish water from 1 dpf to prevent melanogenesis. The mounting procedure for *in vivo* two-photon imaging was described previously.[74] Briefly, zebrafish larvae were embedded in 1.5% w/v low gelling temperature agarose (Sigma-Aldrich, A9414), placed on a microscope slide oriented dorsal side up and submerged in fish water. To prevent movement, α-bungarotoxin (1 nL of 2 mg/mL; Tocris, catalog no. 2133) was injected into the ocular muscles behind the eye. For all experiments in this study the following previously published transgenic lines were used: *Tg(elavl3:H2B-GCamP6s)*,[79] *Tg(opn1sw1:nfsBmCherry)*,[39] *Tg(opn1sw2:nfsBmCherry)*,[80] *Tg(trβ2:Gal4; UAS:nfsBmCherry)*.[81] The previously unpublished *Tg(LCR:nfsBmCherry)* line was provided by Takeshi Yoshimatsu. Outcrosses of the above transgenic lines were performed to co-express the nuclear-localized calcium indicator GCaMP6s at a pan-neuronal level and the nfsB gene in each cone type. Embryos positive for the transgenes obtained from these outcrosses were isolated and raised to adulthood following standard procedures.

METHOD DETAILS

Two-photon calcium imaging and visual stimulation

Imaging during visual stimulation was performed with a Movable Objective Microscope (MOM)-type 2P microscope [designed by W. Denk, Max Planck Institute (MPI), Martinsried; purchased through Sutter Instruments/Science Products] equipped with a mode-locked Ti:Sa laser (Chameleon Vision-S, Coherent) tuned to 920 nm for GCaMP6s excitation and a water immersion objective (W Plan-Apochromat 20x/1.0 DIC M27, Zeiss). For image acquisition, we used custom-written software [ScanM, by M. Mueller (MPI, Martinsried) and T. Euler] running under IGOR Pro 6.3 for Windows (WaveMetrics). Zebrafish brains were imaged at 1.95 Hz (256x256 pixels, 2 ms per line, 0.87 μm/pixel). For visual stimulation, we custom-built a four-colour hyperspectral spatial stimulator based on a previous design[11] with new custom software (see below). The four LEDs used were as follows (from 'red' to UV): B5B-434-TY, SMB1N-D470-02, SMB1N-420H-02 (all from Roithner), and LZ1-00UV0R (LuxiGen). The LEDs were equipped with the following band-pass filters: FF01-586/20 (Semrock), ET480/40x (Chroma), ET420/40m (Chroma), and FF01-370/36 (Semrock), respectively, to restrict the LED emission spectrum to a narrow band for selective cone excitation. Effective LED spectral peaks as measured at the sample were 587, 470, 422, and 373 nm, respectively. To time-separate scanning and stimulating epochs, LEDs were synchronized with the scan retrace at a line-rate of 500 Hz. Each LED's intensity was measured and adjusted to follow the relative distribution of the four wavelength peaks of daytime light in the zebrafish natural habitat (from 'red' to UV: 1200, 600, 300, and 150 $\mu W/cm^2$). The stimulus sequence described below was projected onto a custom screen based on 63gsm tracing paper (3 cm wide and 1.9 cm high, 1.6 cm from the fish) and presented monocularly. Visual stimuli were executed using the Python software QDSpy (RRID:SCR_01698, see below) as follows: static gratings (9.5° wide, 5 s), gratings moving backwards (9.5° wide moving at 46 °/s, 5 s), static gratings (5 s), dark screen ('Off', 10 s), light dots (three bright dots, 4.6° each, bouncing on top of the dark screen in random trajectories at 46 °/s, 5 s), Off (5 s), bright screen ('On', 10 s), dark dots (three dark dots bouncing on top of the bright screen, 5 s), On (10 s). Total stimulus duration was 55 s, and this sequence was presented 6 times. To limit the influence of time-dependent effects, the first repeat was excluded from analysis.

QDSpy

QDSpy is an open-source software package for visual stimulation[11] that runs under Python3 (https://github.com/eulerlab/QDSpy). QDSpy stimuli are written as normal Python scripts that utilize functions from the 'QDS' package to define stimulus objects, set colours, start movies, send trigger signals, and control presentation and display settings (for details, see Franke et al.[11]). For the current study, the software was adapted to present spatial visual stimuli with up to 6 independent 'colours' channels simultaneously. To this end, it controls two DLP (digital-light processing) projectors ('LightCrafter', DLPLCR4500EVM, Texas Instruments) equipped with custom LEDs via a light guide (see above). The projectors' optical paths were combined with a dichroic mirror (T400LP, Chroma, F79-100) to co-project their images onto the screen. One projector generated the RGB, the other the UV stimulus components. For stimulus presentation in dual-display configuration ('screen overlay mode'), the software opens a window that spans both LightCrafter displays and draws the stimuli separately with the appropriate colours onto the two window halves. To ensure that the projector's built-in video circuits do not change image colours or produce scaling artifacts, the projectors were run in 'pattern mode' (which allows exact control over image generation and bit depth) and at the DMD's native spatial resolution (912 x 1,140 pixels).

Please cite this article in press as: Fornetto et al., Zebrafish use spectral information to suppress the visual background, Cell (2025), https://doi.org/10.1016/j.cell.2025.10.009

Two-photon data analysis

Preprocessing, ROIs, and quality filtering

Recordings were detrended and regions of interest (ROIs) were placed as described previously.[69,84] In brief, we used cell-lab[84] to segment all somata within a recording plane, and in parallel computed a response-correlation projection of the entire stack, where each pixel is correlated with each of its immediate neighbours to estimate their response coherence over time.[69] Only ROIs that fell within a single soma-sized segment and that passed a minimum response coherence threshold of 0.1 were considered for further processing. We then extracted each ROI's brightness over time and z-normalized each based on their baseline activity 5 s before stimulus presentation. To limit the effect of time-dependent effects, the first (of 6) response loop was discarded. From here, we optionally applied a combination of response and quality criteria for different analysis, as detailed individually below. First, we computed a response quality index (QI) following Baden et al.[84], which for each ROI and all of its repeats quantifies the mean of the response variance divided by the variance of the response mean. The resulting index varies between 0 (perfectly random) and 1 (all responses identical), and we used QI>0.5 for inclusion. Second, we computed relative response amplitudes to individual stimulus segments relative to a ROI's peak response to any stimulus aspect (=1). Only responses with response amplitudes (RA) >0.5 were included. Where relevant, response amplitudes were additionally related across different 'colour' stimuli in the same way (i.e. RA = 1 denotes the peak response to any stimulus aspect in any colour). Third, we used the spatial location of ROIs within the brain. For this, we defined the centre of the contralateral or ipsilateral tectum (position 0,0), and only included ROIs within a radius of 80 pixels (69.6 μm).

'Population averages' (e.g. Figure 1G) were computed based on QI>0.5 without further amplitude filtering, but only for ROIs within the spatial definition of the contralateral or ipsilateral tectum (see above), as indicated. Traces shown simply reflect the sums of all ROIs that pass the above criteria.

'Brain maps' (e.g. Figure 1H) were computed based on QI>0.5 and RA>0.5 without spatial filtering. Maps were computed based on the original pixel grid of the recordings (i.e. 256x256). For each included ROI across all fish, we added its RA to its spatial location. For better visualization, we applied x3 spatial binning followed by a 3-pixel SD box smooth to each map.

'Trace heatmaps' (e.g. Figure 1I) depict all extracted ROI's z-normalized average response traces within the specified spatial regions of the brain. No QI or RA filtering was applied. ROIs were sorted first by their responses to gratings and bright dots and their relative amplitudes (top), followed by dark-dot dominant responses (middle) and then Off and On-dominant responses, as indicated (bottom).

'*Response Boxplots across colours*' (e.g. Figure 1J) are based on QI>0.5 and RA>0.5 and shown for contralateral ROIs only. In each case, plots show the number of ROIs responding to a given stimulus aspect as indicated (e.g. gratings) relative to the total number of ROIs included.

'*Responses per fish*' (e.g. Figure 2A) denote the total number of contralateral ROIs with QI>0.5 during white stimulation, minus the corresponding number of ipsilateral responses.

'Response percentages' (e.g. Figure 2E) shows the number of contralateral minus ipsilateral ROIs with QI>0.5 and RA>0.5 per fish, normalized across all five stimuli (=100%). Note that this representation accentuates small response numbers (e.g. see red ablation). For non-normalized brain wide number of responses see each corresponding supplemental panel.

'*ROI-wise response amplitudes across colours*' (e.g. Figure 4A) are based on contralateral ROIs across all fish, with QI>0.5 with no amplitude filtering. Each ROI's responses were amplitude-normalized to 1 across all colours.

'*Across-fish correlation*' (Figure 4G) was computed based the distribution of 'response percentages' (see above) across the five stimulus aspects (i.e. gratings, bright dots etc.). For controls and each ablation condition, we computed the correlation coefficient between the distribution of its five response aspects of each fish against the mean of all other fish. Accordingly, a perfectly homogeneous response distribution across the population of fish would yield a correlation of 1, while a perfectly random population would yield 0.

Cone ablations

To selectively ablate *nfsB*-expressing cones, zebrafish larvae were screened for the expression of the co-expressed fluorescent protein mCherry in the eye and treated with Metronidazole (Met; Sigma, M3761) as described previously.[39] In brief, cone ablation was induced at 5 *dpf* by immersing larvae in fish water containing 10 mM Met for 2 hours for acute PR4 ablation; 5 mM Met for 1 hour for acute ablation of PR1 and PR3; 10 mM Met for 1h for acute PR2 ablation. Following Met treatment, zebrafish were transferred into fish water without Met and fed regularly until used for 2P imaging and behavioural experiments at 6-8 *dpf*.

DNA extraction and genotyping

Pairs of primers were designed based on the plasmids used to generate the nfsB-expressing transgenic lines, to selectively amplify different DNA sections simultaneously. These custom primers were used in the polymerase chain reaction (PCR) to isolate larvae expressing the nfsB gene in multiple cone types, subsequently employed in double and triple cones ablation experiments. The sequences of each pair of primers were as follows: sw1:nfsBmCherry (forward 5'-TCAAGAAACTCGTGAGGGGT-3' and reverse 5'-TCAACAACCAGCTTCAGCCA-3', product length 773 bp); sws2:nfsBmCherry (forward 5'-GCTGGTGACAACAAACCTCA and reverse 5'- GTGCGAGGCATCAAGCATTT-3', product length 552 bp); LCR:nfsBmCherry (forward 5'-GCAAATGTCCTAAAT GAATTTGTGT-3' and reverse 5'- ATAAAATGCCACGGCTGGGA-3', product length 435 bp); trβ2:Gal4 UAS:nfsBmCherry (forward

5'- TGCGCCAAGTGTCTGAAGAA-3' and reverse 5'- TCCGATGATGATGTCGCACT-3', product length 320 bp). Outcrosses between adult zebrafish expressing Tg(elavl3:H2B-GCaMP6s; opn1sw2:nfsBmCherry) and Tg(elavl3:H2B-GCaMP6s; LCR:nfsBmCherry) were performed. The embryos obtained by this outcross positive for the transgenes (judged by the co-expression of GCaMP in the brain and mCherry in the eye) were isolated and raised to adulthood. Once adult, a genomic DNA extraction was performed to isolate fish expressing the nfsB gene in both PR2 and PR3. Genomic DNA extraction from adult zebrafish was performed by caudal fin clipping.[85] Animals were anesthetized in Tricaine 25X (4 g/L; Sigma, A5040) and the caudal fin was removed using a scalpel blade. The tissue was then transferred into a reaction tube (Eppendorf) containing 100 μL of 50 mM NaOH (Sigma, 221465), heated to 95°C for 20 min and then cooled to 4°C. To neutralize the basic solution 10 μl of 1 M Tris-HCl, pH 8.0 was added (1/10th of initial volume) followed by a centrifugation at 12000 rcf, 25°C for 5 min, so that the supernatant was ready for use in PCR. To select fish for double cone ablation we used multiplexed PCR, thus amplifying different DNA sequences in one reaction using multiple pairs of primers. For 25 μL reaction with two primers pairs the following reagents were used: 0.5 μL of 10 μM forward primer_1, 0.5 μL of 10 μM reverse primer_1, 0.5 μL of 10 μM forward primer_2, 0.5 μL of 10 μM reverse primer_2, 4 μL DNA sample, 12.5 μL OneTaq Quick-Load 2X Master Mix with Standard Buffer (Biolabs, M0486S), 6.5 μL Nuclease-free water. Reactions were amplified using the following conditions: 94°C for 30 s; 30 cycles of 94° for 30 s, 58°C for 1 min, 68°C for 1 min; followed by 58°C for 5 min. 7 μL of each reaction were loaded onto a 2% agarose gel prepared mixing 2 g agarose (Meridian bioscience, BIO-41025),100 mL TAE 1X (Tris-Acetate-EDTA, pH 8), 2.5 μL SYBR Safe DNA Gel Stain (S33102, Invitrogen) and electrophoresed at 90V for 40 min in TAE 1X. We also loaded 2 μL low range DNA ladder (Meridian bioscience, BIO-33056). The gel was imaged using a ultraviolet (UV) transilluminator apparatus (Odyssey XF, Licor). The bands matching the target size of 435 bp and 552 bp indicated the presence of nfsB-mCherry construct in PR2 and PR3, respectively. These fish were then incrossed, screened and raised to adulthood and subsequently outcrossed with wild-type fish and genotyped to isolate the homozygous for *nfsB*-mCherry in PR2 and/or PR3.

For the other cone ablation combinations (e.g. PR1/4 double ablation, PR1/2 double ablation, PR2/4 double ablation, PR1-3 triple ablation, PR2-4 triple ablation) we followed Wilkinson and colleagues' method for genotyping of live larval zebrafish.[86] Positive larvae obtained by the outcrosses of the transgenic lines for the above-mentioned cone ablation combinations were screened (judged by the co-expression of GCaMP in the whole brain and mCherry in the eye) and isolated for genotyping at 2 *dpf*. Larvae were anesthetized in Tricaine 25X, placed under a stereomicroscope, and the tip of the caudal fin was removed using a 20g needle. The larvae were then transferred in Petri dishes with fish water and kept at 28°C to allow caudal fin regeneration and their normal development. The fin tissue was transferred into a reaction tube (Eppendorf) containing 50 μL of 50 mM NaOH (Sigma, 221465) using a glass pipette, heated to 95°C for 10 min and then cooled to 4°C. To neutralize the basic solution 5 μl of 1 M Tris-HCl, pH 8.0 was added followed by a centrifugation at 12000 rcf, 25°C for 5 min. A multiplexed PCR was performed as described above, but in this case 6 μl of DNA sample were added to the reactions (instead of 4 μl) as well as two or three pairs of primers based on the cone ablation combinations needed. Reactions were amplified and electrophoresed as described above. The bands matching the target size of 320 bp, 435 bp, 552 bp and 773 bp indicated the presence of nfsB-mCherry in PR1-4, respectively. The samples expressing nfsB-mCherry in two and three cone photoreceptors were used for 2P imaging and behavioural experiments at 6-8 *dpf* after Met treatment at 5 *dpf*. Larvae not used for experiments were raised to adulthood.

Indoor Optomotor assay and spontaneous swimming

Behavioural assays were performed on individual larvae (6-8 *dpf*) using a closed loop optomotor setup as described previously.[43] Freely-swimming larvae were placed in a 6 cm diameter watch glass in filtered fish water. Swimming behaviour was recorded at 200 Hz using a high-speed camera (Omron Sentech STC-CMB200PCL-NIR, Alrad Instruments Ltd, UK) connected to a digital frame grabber (Euresys Grablink Full XR, Stemmer Imaging, Germany) equipped with a zoom lens (Thorlabs, MVL8M23) and infrared (IR) filter (Thorlabs, FELH0750). The arena was illuminated by an IR LED (Thorlabs, M850L3) from below. Stimuli were projected onto a diffuser screen from beneath after reflection by a 5 cm diameter cold mirror (Thorlabs, FM203) using a commercial DLP projector (VAMVO Ultra Mini Portable DLP Projector, 1920x1080 pixels, Shenzhen, China). All experiments were performed in the dark at 28°C. Animals were allowed to adapt to the arena and light conditions for at least 15 minutes prior to each behavioural test. One larva at a time was tested and the same fish were used both for spontaneous and OMR behaviour. For spontaneous swimming we tracked fish both in the dark and in white (RGB) light, 3 minutes each. For optomotor behaviour, image processing and stimulus generation were performed in Bonsai using the BonZeb package.[82,83] Widefield sinusoidal gratings of 1 cm spatial frequency moving at 1 cm/s were presented for 30 s. A closed-loop assay was performed where the orientation of the drifting gratings (calculated using the heading angle of the fish) updated in real time running parallel relative to the fish body axis. Each trial started with a 30 s grey screen, followed by 60 s of gratings drifting rightwards and leftwards (30 s per direction). This protocol was repeated three times, and each session lasted about 5 min. Each recording was then down sampled to 50 Hz, and all subsequent analysis was performed using custom-written Igor Pro 9 scripts (WaveMetrics). Bouts and turns were detected by thresholding each fish's movement and turn traces over time, with thresholds of 3 pixels/s (~180 μm / s) and 0.2 radians/s respectively. The exact choice of these thresholds did not qualitatively affect the results. Shown are either the total number of bouts or turns across the full recording (i.e. 3 times 30 s = 90 s), or the corresponding numbers normalized by those of control animals, as indicated. The optomotor index was computed from across both motion directions (see above), as (C-I)/(C+I), where C and I denote the number of correct (towards stimulus) and incorrect turns, respectively.

Please cite this article in press as: Fornetto et al., Zebrafish use spectral information to suppress the visual background, Cell (2025), https://doi.org/10.1016/j.cell.2025.10.009

Outdoor optomotor assay

Zebrafish larvae (*6-8 dpf*) were placed in a custom-built behavioural rig placed outside in the sun (UK weather permitting, cf. Figures 6D, 6E, and S7A). This setup was based around an open-top 45 L glass aquarium (50 × 30 × 30 cm). To limit reflections and to restrict illumination to overhead only, the four sides of the aquarium were covered with black panels (Thorlabs, TB5). A fifth black panel with a rectangular opening for stimulus display (35 × 15 cm) was placed beneath. The aquarium was filled with fish water to 25 cm depth, and the temperature was kept at 29°C using a 50W heater. Freely-swimming larvae were placed in a 9 cm Petri dish in fish water. Specifically, the dish was placed in a 3D printed holder in the middle of the aquarium, centred above the rectangular hole (Figure 6E) and half submerged in water, ensuring that the distance between the fish and the stimuli was 25 cm. A 3D printed separator was used to split the Petri dish in half allowing to simultaneously record controls and cone ablated fish (genotyped at 2 dpf as described above), about 25 fish per side. Newly positioned animals were allowed to acclimatize for 15 mins prior to experiments, and 10 mins between trials. Stimuli were presented from below using a custom-built motorized conveyor belt, based on 3D printed parts and 1.5 × 1.5 cm rails (MakerBeam). For the stimuli, light and dark stripes (10° when viewed from a distance of 25 cm) were produced by gluing LeeFilters (#787) strips onto an A3 white paper. Spectra of both light and dark bars were measured using a spectrometer (Thorlabs, CCS200, Figure S7C). Stimuli were presented by moving the bars at a speed of 20°/s using the Nema17 stepper motor (driven by l298 H-bridge), connected to a 10 kΩ potentiometer and 9V 1A battery, all controlled by an Arduino Uno. An open-loop assay was performed by moving the bars for 30 s in one direction and 30 s in the opposite direction for 3 times (see also Video S3). Optomotor behaviour was recorded in both clear and tinted water. The latter was realized by adding food dyes (red and blue, spectra resultant spectra shown in Figure S7C). These spectral distortions were introduced to approximate different naturalistic water conditions – note that despite their very different overall shapes, spectra were still wide and without gaps. Behavioural variance attributable to different water conditions was below the natural variance across experimental days and batches of fish (shown separately in Figures S7D–S7G).

Animals were filmed at 10 Hz using a camera (Basler, ACa1440-200um USB 3.0 camera, 1.6 MP) positioned above and equipped with an objective (Fujinon, DV3-4x3-8SA-1 F1.4 f3.8-13mm 1/2") and infrared filter (850 nm, MaD Cameras). Additional infrared illumination (beyond the light provided by the sun) was presented from above using an LED panel to limit shadows provide a homogeneous illumination. Animal tracking was performed in Fiji. Fish positions were used to calculate a running Preference Index (PI) as the difference between the number of fish in the right and left half of the Petri dish divided by the total number of fish (Figure 6F). From here, we then quantified the 'population optomotor response' (population OMR) as the mean position of all fish in the dish over time, corrected for stimulus direction and excluding each first 15 seconds following stimulus reversals. In parallel, we also computed a population heterogeneity index by quantifying the mean squared error between each individual experimental run and the mean of all other runs (such that 0 indicates zero variation across the population).

Phototaxis

Zebrafish larvae (6-8 *dpf*) were tested for phototaxis in a custom-built behavioural rig, with ten freely-swimming larvae placed in a 5 cm diameter Petri dish in filtered fish water. The Petri dish was placed on a custom 3D printed holder with a separator in the middle to allow the illumination only in one half of the dish. Animals were tracked at 30 Hz using a camera (Basler, ACa1300-200um USB 3.0 camera, 1.3 MP) positioned above and equipped with an objective (Basler, Ricoh Lens FL-CC0614A-2M F1.4 f6mm 2/3'') and an IR filter (760 nm, Zomei). Infrared illumination and light of different wavelengths were projected from below onto a diffusing screen. For stimulation we used four LEDs (from 'red': Thorlabs, LED591E; Roithner, RLS-5B475-S, VL415-5-15, XSL-365-5E) located both on the left and the right side below the dish so that they were properly collimated and aligned covering the entire half-dish. All the LEDs were controlled using an Arduino Mega with custom scripts. The intensity of each LED was adjusted to 6 $\mu W/cm^2$ on the sample. All experiments were performed in the dark and at a controlled temperature of 28°C. Animals were allowed to adapt to the arena and light conditions for at least 15 minutes before starting the behavioural tests. Visual stimuli were presented alternately on one side of the dish for 30 s, three times per side (each session lasted 3 min, see also Video S4). We waited at least 5 minutes prior to the presentation of the next stimulus (i.e. different wavelength light). Each recording was then down sampled to 1 Hz and multi-animal tracking was performed using the Fiji *mosaic* plugin. Fish positions were used to calculate a running Preference Index (PI) as the difference between the number of fish in the lit side and the dark side divided by the total number of fish. From here, we calculated a phototaxis index per dish (of 10 fish) and trial based on the average PI between 10 and 30 seconds into each stimulus switch (i.e. leaving out the first 10 seconds, while fish were mostly still moving). The exact choice of this time window did not qualitatively affect the results. Analyses were performed with custom-written MATLAB and Igor Pro 9 scripts.

Natural scene processing

Video S1 shows a luminance-calibrated RGB underwater video of the zebrafish natural habitat based on Alexander et al.[87] where a robotic gantry system was used to gradually advance the camera through vegetation over a distance of ~ 30 cm was used. Water depth was ~50 cm. For processing, brightness was calculated as the sum of the three spectral channels, while 'spectral width' ('whiteness') was computed per frame and pixel, as 1 minus the standard deviation divided by the mean across the three spectral channels. In this way, a pixel with equal red, green and blue values yield a 'whiteness' of 1 (independent of brightness), while unequal values across the three channels yield correspondingly lower values. Notably, there are many ways that could be used to estimate spectral width from RGB video data, but because these all yield qualitatively similar results, we opted to use this very simple metric.

Activation of opponent and non-opponent channels as a function of decreasing whiteness (Figures 1A and 1B) was computed based on the simplifying assumption that full-spectrum illumination is spectrally sinusoidal from 0-π (cf. Figure 1A), gradually narrowing along a triangle formed from 0 and π towards a monochromatic point at 0.75 * π. 'Whiteness' (*x* axis in Figure 1B) is then computed as the full width half maximum of this model spectrum. Spectra were then multiplied with a same frequency and phase-aligned $\sin^2$ function to mimic non-opponent drive (Figure 1A, middle), and a correspondingly frequency-doubled $\sin^2$ function for opponent drive (Figure 1A, right). Normalized activation was then computed as the area under the curve relative to zero in each case, divided by the largest entry across whiteness conditions in each case.

Modelling of cone drive

(Figures 4A–4F). To estimate the underlying cone contributions that led to the spectral tuning functions of grating responses and bright dot responses following PR2/3 double ablation and in controls, we set up a cone-combinatorial model. PR1 and PR4 contributions were fitted to the tuning functions from PR2/3 ablated animals, while independently the contributions from PR2 and PR3 were estimated based on the differences in spectral tunings functions between controls and PR2/3 double ablated animals. Except for these spectral target functions, and the cone pairs used to fit them, the remainder of the modelling was identical, and will therefore only be described once, using the example of PR1/4 fitting for gratings (Figure 4C) as an example.

We used the previously determined[15] spectral tuning functions of the cones as the input (shown in Figure S1B and converted to expected activations for the stimulus combinations in this present work in Figures S1D and S1E). First, we computed the sum of both cones' tunings for all possible cone ratios (i.e. r*PR1 + u*PR4, where r and u each varied between -1 and 1.), and mapped them onto a circle indicated as 'linear' around the origin of the heatmaps shown, such that r;u = 1;0 and r;u = 0;1 were mapped to the right and top of the circle, respectively. The four quadrants therefore represent all possible positive sums (top right), negative sums (bottom left) or opponent contributions (top left, bottom right), while the axes represent pure cone contributions (e.g. right is +PR1 only, top is +PR4 only, and so on). We then computed corresponding nonlinear versions of the same basis functions by raising them to the power of *nl*, which ranged from 0 to 5. Accordingly, *nl*<1 gave sublinear scaling, while *ln*>1 gave supralinear scaling. This nonlinearity *nl* was mapped along the radial dimension as indicated. Based on this spatial mapping, we then shaded each pixel by the mean squared error (MSE) between each resulting template function and the target tuning function as defined by the corresponding brain responses (cf. Figures S4E–S4H). MSEs were normalized to the error score resulting from a fit with all entries at zero, such that MSE = 0 indicates a perfect fit, while MSE =>1 indicates that the fit was equal than or worse than no fit at all. In each case, the fit with the lowest MSE overall (filled symbol) and the lowest MSE of a linear model (open symbol) are indicated.

QUANTIFICATION AND STATISTICAL ANALYSIS

No statistical methods were used to predetermine sample size. Owing to the exploratory nature of our study, we did not use randomization or blinding. We used 1- and 2-tailed paired and non-paired Wilcoxon Rank Sum or t tests with Bonferroni correction for multiple comparisons for all statistics, as appropriate and individually indicated.

CellPress
OPEN ACCESS

Supplemental figures

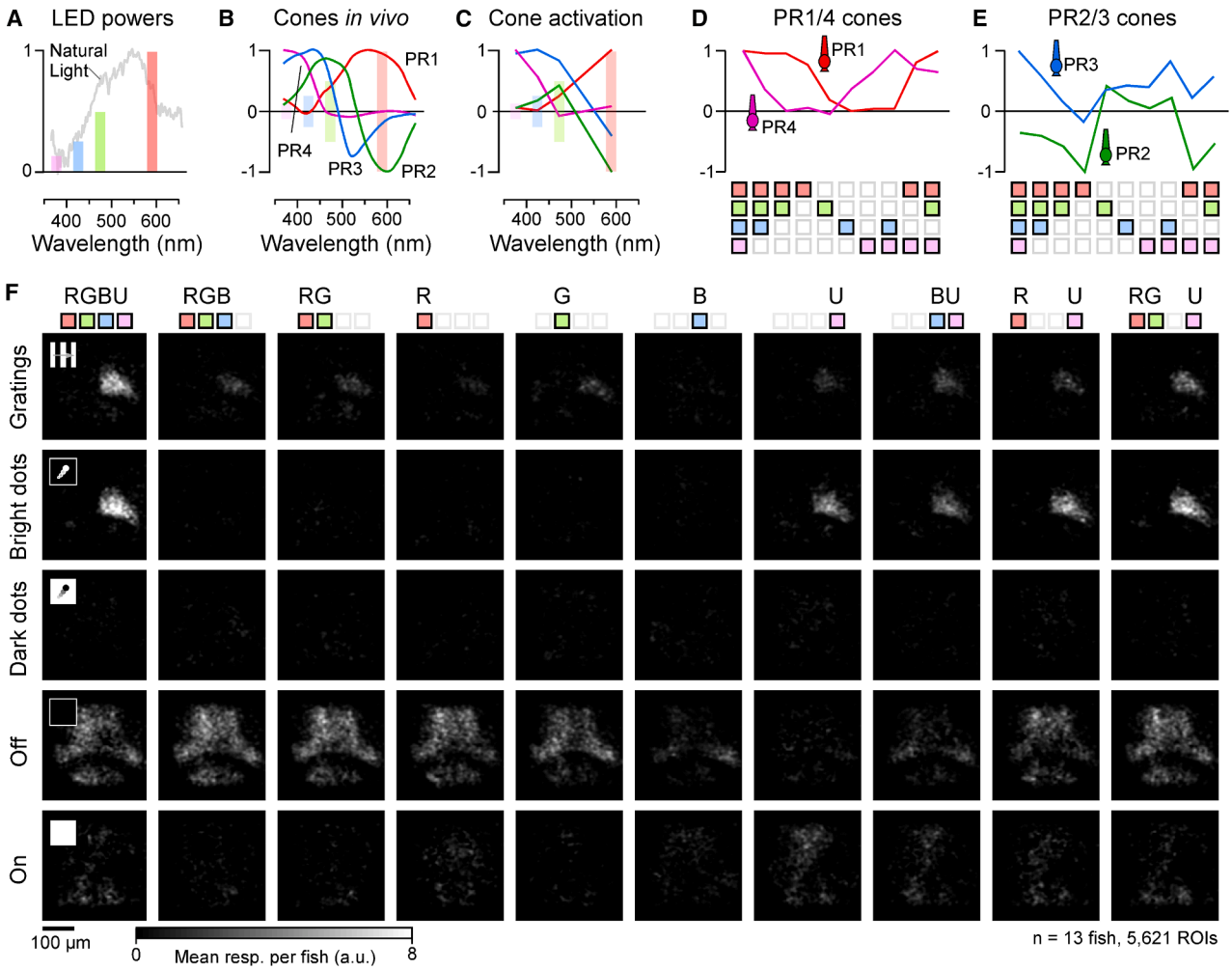

Figure S1. Spectral properties of stimulation LEDs and corresponding cone activations in larval zebrafish, related to Figure 1

(A) Spectral centers and relative powers of light-emitting diodes (LEDs) used for stimulation, with the mean spectrum of natural daylight in the zebrafish natural habitat superimposed.[30]

(B–E) Spectral sensitivities of larval zebrafish cones *in vivo* (B, from Yoshimatsu et al.[15]) superimposed on LEDs, the cones' spectral sensitivities at the LED positions multiplied by their respective powers (C), and corresponding cone activation patterns for presented LED combinations (D and E, cf. Figures 1C–1J).

(F) As in Figure 1H for presented LED combinations.

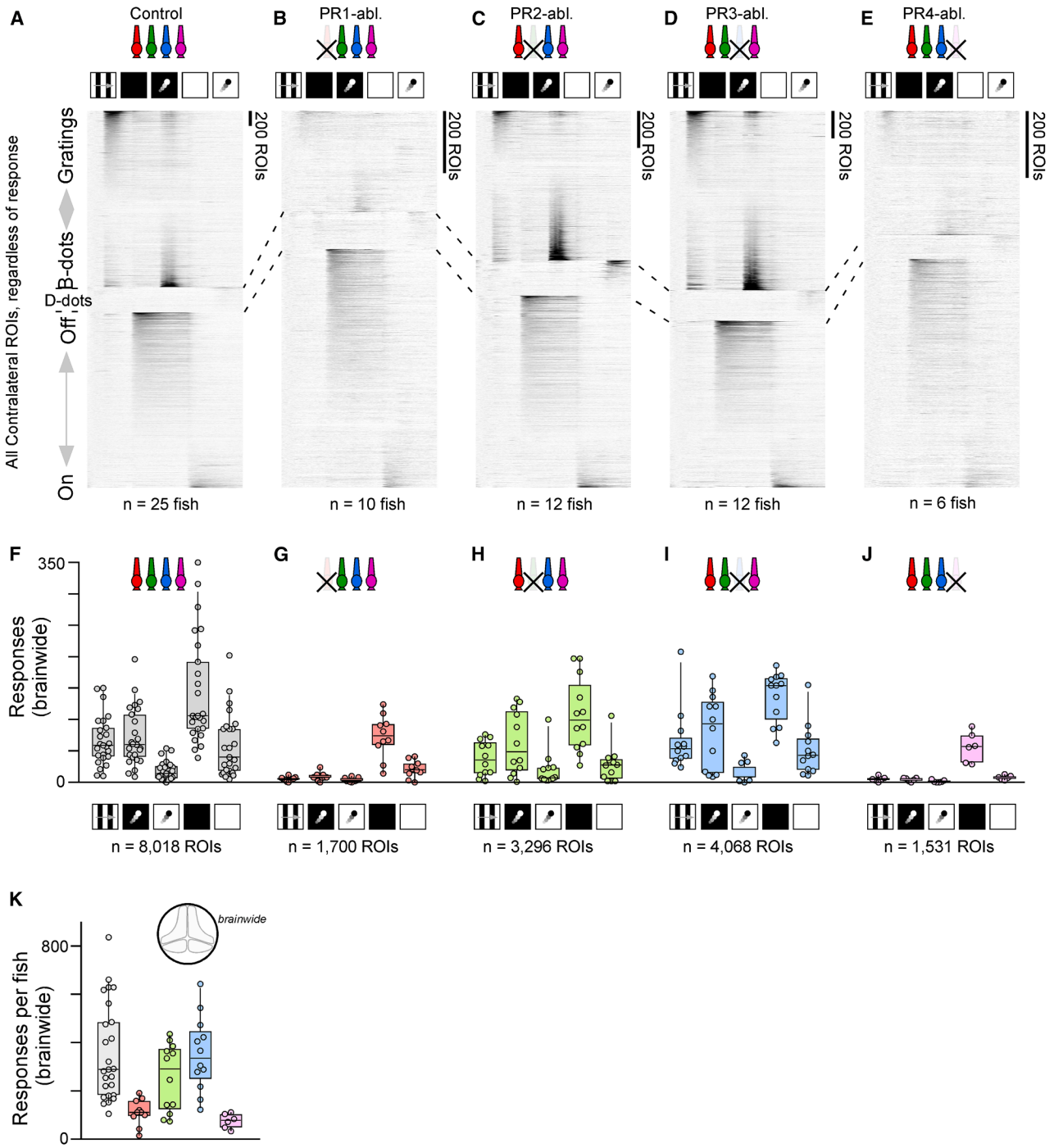

Figure S2. Effects of selective PR ablations on brain-wide responses, related to Figure 2

(A–E) As in Figure 1I, shown for white-only stimulation of controls (A) and following ablation of cone types: PR1 (B), PR2 (C), PR3 (D), and PR4 (E).

(F–K) As in Figures 2E–2I and (A), respectively, shown for uncorrected numbers of brain-wide responses.

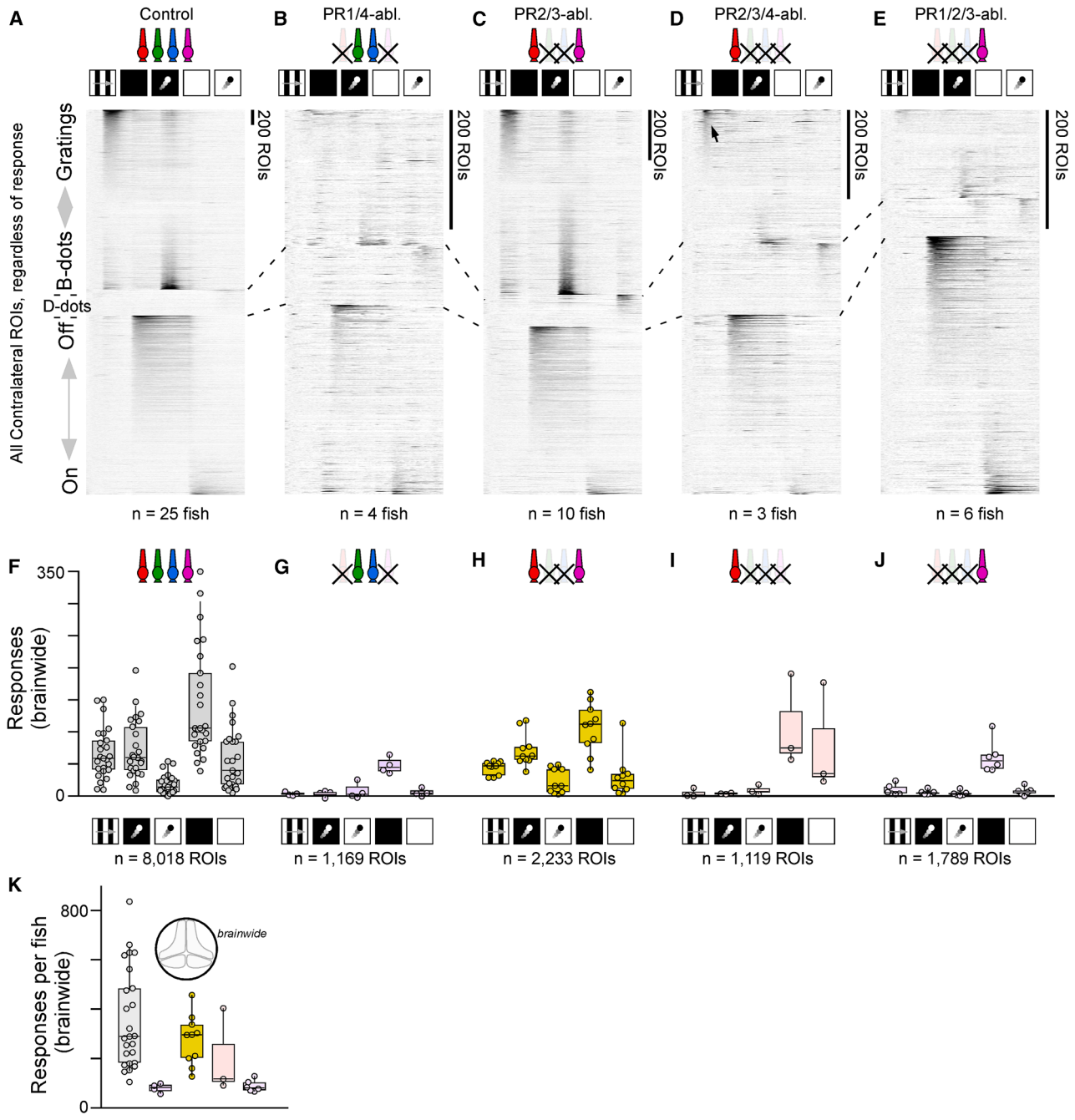

Figure S3. Effects of double- and triple-PR ablations on brain-wide responses to white stimulation, related to Figure 3

(A–K) As in Figures S2A–S2K, shown for cone ablations as shown in Figure 3.

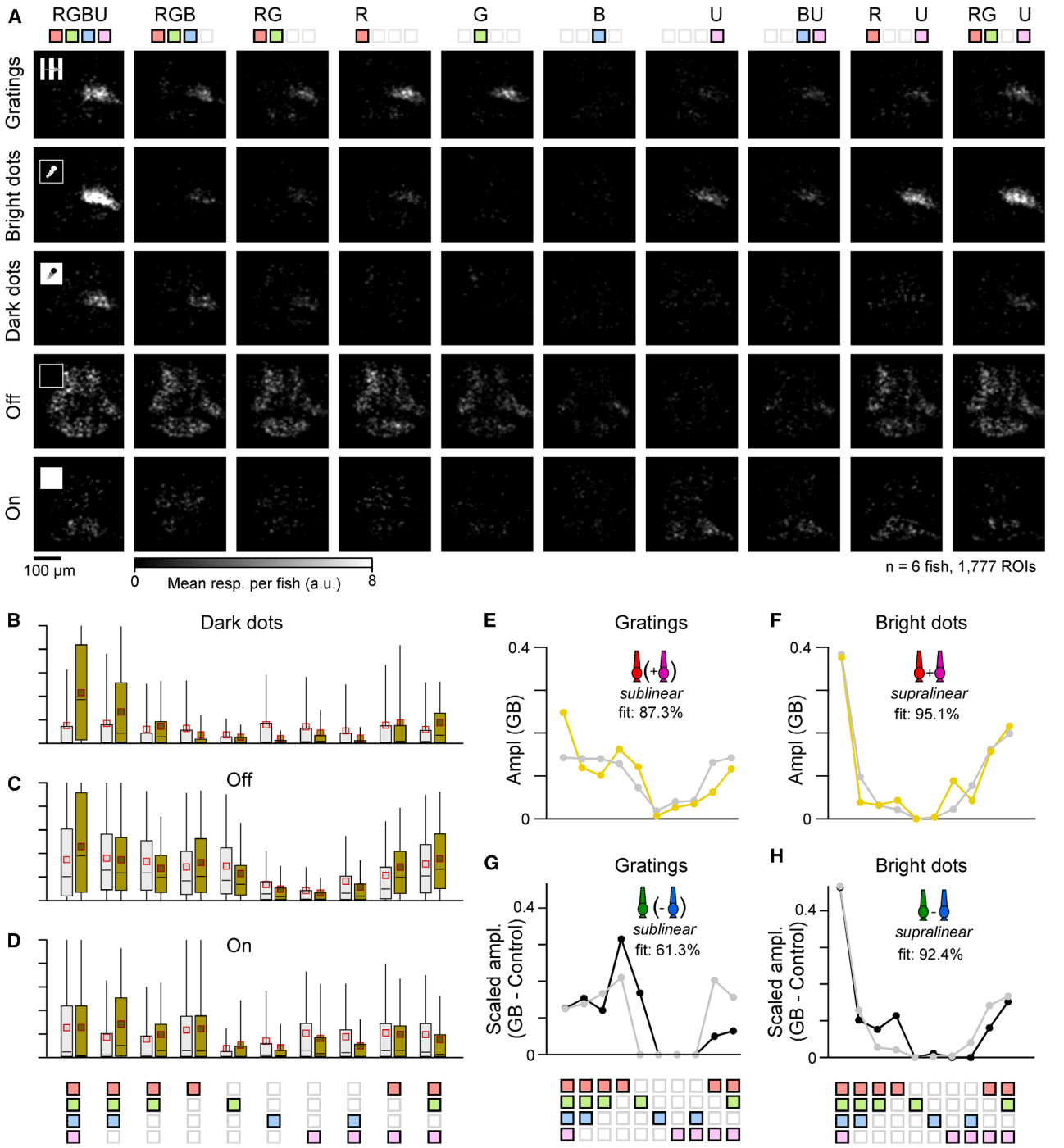

Figure S4. Model fits and tuning functions after PR2/3 double ablations, related to Figure 4

(A) As in Figure S1F, shown for PR2/3 double ablation.

(B–D) As in Figures 5A and 5B, shown for the remaining three stimuli.

(E–H) Related to Figures 4C–4F, corresponding best model fits (gray) superimposed on respective target-tuning functions (yellow/black). Indicated fit quality based on the residual mean squared error (MSE) of the best fit as shown, compared with the fit with all entries = 0.

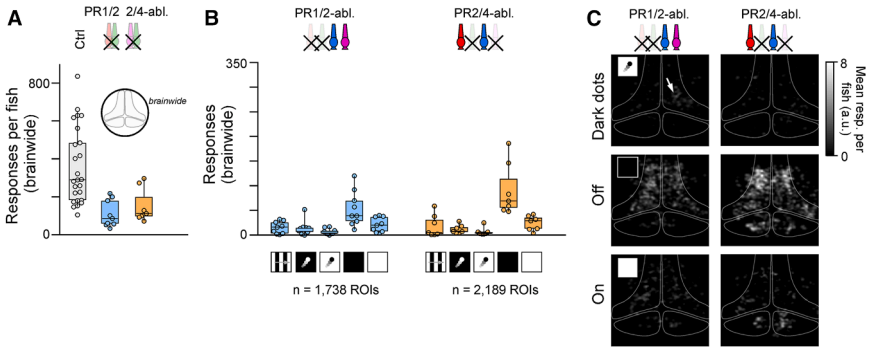

Figure S5. Brain-wide responses to white-light stimulation following PR1/2 and PR2/4 ablation, related to Figures 4G–4M

(A–C) As in Figures S2F, S2K, 2D, and 3D, shown for the ablation combinations as in Figures 4H–4M.

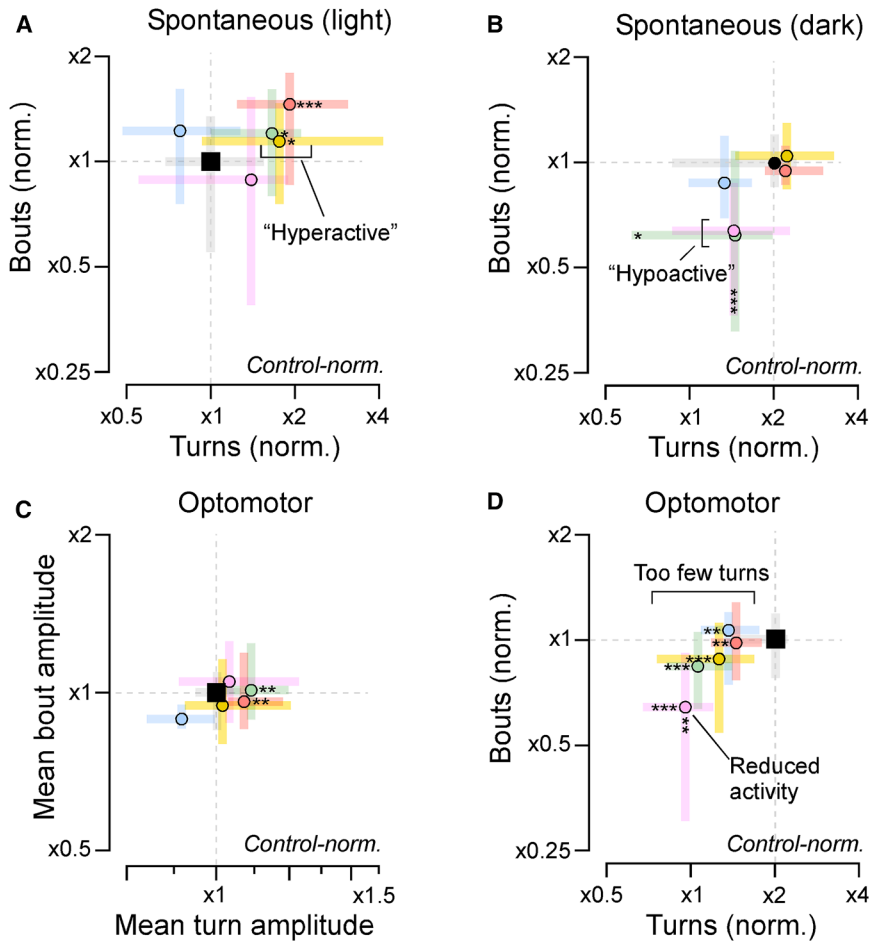

Figure S6. Behavioral kinematics in spontaneous swimming and optomotor stimulation, related to Figures 5 and 6

(A and B) As in Figures 5E and 5F, for normalized bout and turn rates in the light (A) and dark (B). Full statistics in Table S2B.

(C and D) As in Figures 5E and (A), respectively, shown for movement statistics during optomotor stimulation (full statistics in Table S2B).

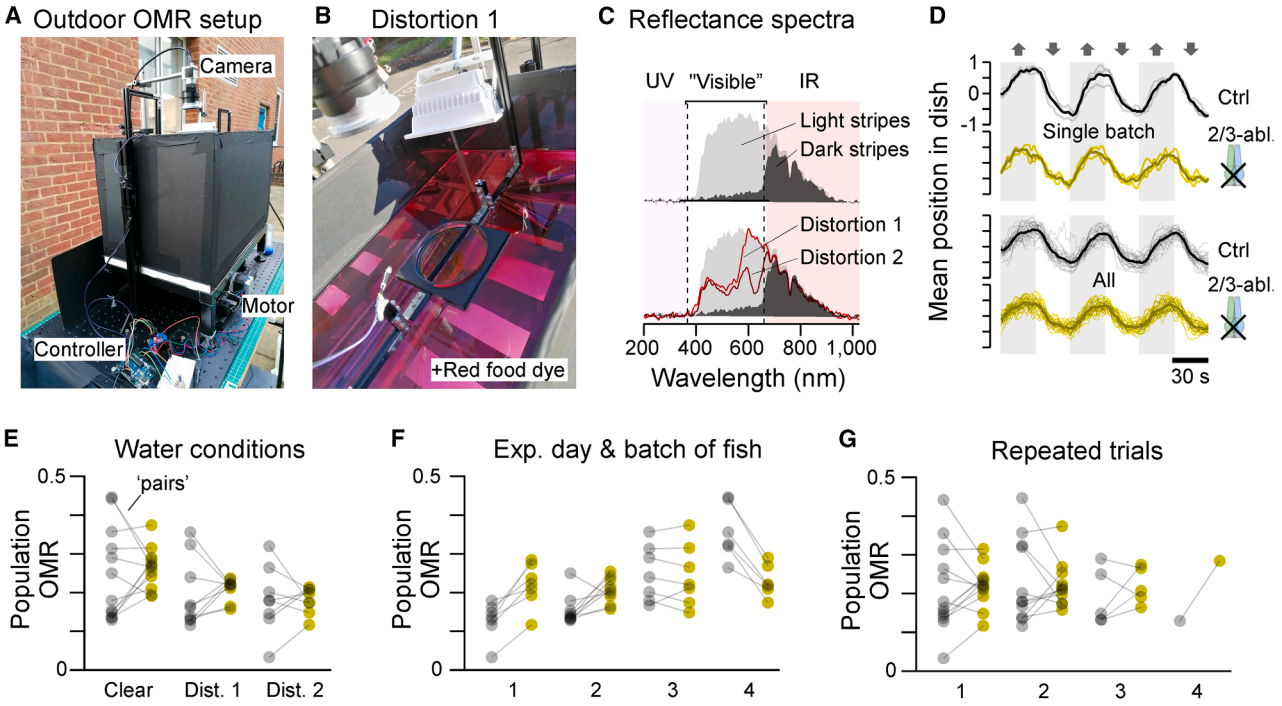

Figure S7. Outdoor-optomotor setup and spectral distortions, related to Figure 6

(A and B) Photographs of outdoor-optomotor setup, showing the full system (A) and a close-up after adding red food dye to the water (distortion 1; STAR Methods).

(C) Natural sunlight reflectance spectra measured as seen by the fish, for dark and light stimulus bars (top) and for light bars following two spectral distortions (cf. B; STAR Methods). Note that despite distortions, all spectra remained broad from UV to red and without notable spectral gaps.

(D) Average position of all "additional" control and PR2/3 double-ablated fish per side over time. Top: three repeats of one batch; bottom: all experiments ($n = 29$).

(E–G) Optomotor performance sorted by water condition (E, clear water and two distortions), experimental day/batch of fish (F, different batches of fish were used on different days), and repeated trials for individual batches and conditions (G).